Ultrastructural and elemental analysis of sialolith and their comparison with tonillolith and antrolith

타석의 초미세구조 및 성분 분석 ; 편도석 및 상악동석과의 비교 연구

2023 년 2 월

서울대학교 대학원

치의과학과 구강악안면외과학 전공

Buyanbileg Sodnom-Ish

Ultrastructural and elemental analysis of sialolith and their comparison with tonsillolith and antrolith

지도교수 김 성 민

이 논문을 치의과학박사 학위논문으로 제출함

2022 년 10 월

서울대학교 대학원

치의과학과 구강악안면외과학 전공

Buyanbileg Sodnom-Ish

Buyanbileg Sodnom-Ish 의 박사학위논문을 인준함

2023 년 1 월

위 원 장_____명   훈_____(인)

부위원장_____김 성 민_____(인)

위   원_____양 형 철_____(인)

위   원_____서 미 현_____(인)

위   원_____김 민 근_____(인)

Abstract

Ultrastructural and elemental analysis of sialolith and their comparison with tonsillolith and antrolith

Buyanbileg Sodnom-Ish

Program in Oral and Maxillofacial Surgery, Department of Dental Science, Graduate School, Seoul National University
(Directed by Professor Soung Min Kim)

Introduction

Sialolithiasis is the primary etiology of submandibular and parotid gland swelling and pain, with an incidence of 1:15,000 to 1:30,000. Many theories have been proposed on sialolith formation (lithogenesis), such as 1) the organic core theory; 2) the sialomicrolith theory; and 3) the mucoepidermoid gel theory. However, the exact mechanism of sialolith formation is still unknown. Although, there are numerous studies on the characterization of pathological deposits in the human body such as the nephroliths, uroliths, gallstones, and cardiovascular calcifications, very limited data exist on the ultrastructural and elemental composition of sialoliths. By performing a comparative ultrastructural and chemical composition analysis of sialoliths, tonsilloliths, and antroliths, the current study aimed to identify their growth pattern as the first step in developing intervention methods to prevent sialolith formation and its complications.

Materials and methods

Twenty-five specimens obtained from 23 patients were classified into three groups: sialoliths (A), tonsilloliths (B), and antroliths (C). The specimens were examined histopathologically and characterized in detail by micro-CT. For scanning electron microscopy (SEM) and energy dispersive X-ray spectroscopy (EDS) analysis, regions of interest (ROIs) were designated in each specimen's peripheral, middle, and core regions to analyze the local ultrastructure at finer scales. Transmission electron microscopy (TEM) was also performed on specimens from each group. The data's normal distribution was tested by the Shapiro–Wilk test. The differences between groups were tested by one-way ANOVA. $p < 0.05$ was considered statistically significant.

Results

Micro-CT analysis

Group A showed onion skin-like layered structure with alternating radiodense and radiolucent layers in both submandibular and parotid gland sialoliths. In group A, 11 sialolith specimens had a single core, while one sialolith had multiple cores, one sialolith had two cores, and one sialolith with no distinct core. The sialolith cores in group A displayed either distinctively higher or lower degree of mineralization compared to the surrounding layers. The sialoliths had nearly spherical oval, or asymmetrical shapes Group B, the tonsilloliths, had a homogeneous structure without concentric laminated pattern. The group C specimen revealed a compact homogenous structure, with more internal voids compared to that of group A and group B. Although each group showed different morphometric parameters of total VOI (volume of interest) volume, object volume, percent object

volume, total VOI surface, object surface, object surface/ volume ratio, object surface density, structure thickness, structure separation, and total porosity (percent), no statistically significant differences were found.

Histopathological analysis

Group A showed concentric lamellar structure with organic and inorganic substances. A laminated, teardrop-shaped, globular structure was present at the periphery. Group B showed a duct-like structure present at the center of squamous epithelium indicative of the minor salivary gland duct. Squamous epithelium on the surface of the tonsillolith was noted to extend toward the lining of the tonsillar crypt. In group C, the lesion was not encapsulated and showed a homogeneous lamellar bone with fibrous marrow cavities.

SEM analysis

The general architecture of Group A in SEM findings was a concentric lamellar structure with alternating mineralized and organic material. A diatomite was found at the core of the sialolith in a recurrent stone (A17). The BSE mode allowed for the comparison of the different chemical composition in each layer as the probability of electron backscatter was proportional to the atomic mass of the specimen element. The fine structure of each layer was threaded with mineralized globules.

EDS analysis

The compositional analysis of each specimen demonstrated a high fraction of consistent components, calcium (Ca), carbon (C), and oxygen (O), in groups A,

B, and C. Group A had a significantly higher level of Ca wt% (20.50 ± 6.28 wt% and 16.74 ± 44.08 at%) compared to that of Group C (14.78 ± 10.29 wt% and 5.76 ± 4.52 at%) ($p = 0.003$). The C level was higher in group C (49.27 ± 20.21 wt% and 49.27 ± 20.21 at%) compared to that of group A (22.48 ± 11.08 wt% and 33.64 ± 6.36 at%), although no significant difference was found The wt% and at% of O was significantly higher in group A (36.46 ± 8.16 wt% and 40.12 ± 8.93 at%), compared to that of group C (27.18 ± 2.37 wt% 25.36 ± 4.29 at%) ($p = 0.002$; $p = 0.019$, respectively).

Other elements including nitrogen (N), sodium (Na), and silicon (Si) were detected in both groups. Copper (Cu), fluorine (F), phosphorus (P), zinc (Zn), and zirconium (Zr) were found only in group A, while group C did not show these elements. The C level was significant higher in group C (49.23 ± 20.22 wt% and 59.23 ± 18.68 at%), compared to that of Group A (22.36 ± 4.70 wt% and 32.46 ± 5.74 at%) ($p = 0.00$; $p = 0.035$, respectively).

TEM analysis

In group A, globular structures with a double membrane were detected undergoing intra-vesicular calcification. Lipid vesicles and finger-like globular structures were also detected. Needle-like filamentary crystals suggested hydroxyapatite structure. Intra-vesicular and extra-vesicular deposition of inorganic matter was seen. Group B had stratified squamous epithelium in its peripheral area. Bacteria were present in the middle layer and needle-like crystals were seen in the core region. In the outer layer of the group C an osteoblastic rimming was observed. The middle region of the specimen was mainly composed of dense, mature, and

predominantly lamellar bone. The core region had no Haversian canals and fibrous component.

Conclusion

This was a new comparative, ultrastructural and elemental study of different types of calcifications found in the Oral and Maxillofacial Surgery field. The study demonstrated that sialoliths, tonsilloliths, and antroliths have completely different micromorphology and elemental composition as determined by micro-CT, SEM, EDS, and TEM analysis.

The sialoliths had a concentric laminated structure with highly mineralized or less mineralized core, while tonsilloliths and antroliths lacked a core. Antroliths showed a structure and composition similar to that of a lamellar bone. These results suggest a different lithogenesis pattern in each type of calcification. This could be the fundamental step in developing different treatment modalities for each type of calcification.

Content

I. Introduction

Among human calcium phosphate calculi or stones, there exist dental calculus, salivary stones or sialoliths, urinary tract stones or uroliths, and renal stones or nephroliths. In addition, rhinoliths or nasal stones, antroliths or maxillary sinus stones, tonsillolith or tonsil stones, pancreatic calculus, uterine stones, gallstones, and other stones are also known [1]. Kidney stones have been formally studied since 1802. There is extensive study on the pathophysiology, microstructure, chemistry, microbiome composition, prevention and treatment of kidney stone formation [2-8]. A recent study demonstrated a possible comprehensive therapy using apoptosis inhibitor of macrophage (AIM, CD5, CD5L) protein against kidney stone disease occurrence/recurrence [3]. Although there are numerous studies on kidney stones and urinary tract stones, the exact pathogenesis of sialolith, tonsillolith and antrolith are still not completely understood.

I.1. Sialolith, tonsillolith and antrolith formation (lithogenesis)

Sialoliths are calcified masses that are common in the submandibular gland and its duct system. Regarding the anatomical location of sialolith formation, the submandibular gland is the most affected organ (85%) while parotid and sublingual glands are affected in 10% and 5% of total cases, respectively [9] Many theories have been proposed on sialolith formation, which include 1) the organic core theory (calcification of bacteria, foreign body, or desquamated epithelial cells); 2) the sialomicrolith theory (normally present in 80% of submandibular glands); and 3) the mucoepidermoid gel theory (calcification of high viscosity mucins) [10, 11].

The most comprehensive and solid observations are the occurrence of sialomicroliths, which are found in normal salivary glands of asymptomatic individuals [11]. It appears that microscopic secretions known as sialomicroliths accumulate during normal activity of the salivary gland, leading to inflammatory foci which can either be primary or caused by retrograde migration of oral bacteria. Sialomicroliths appear to develop more in the submandibular salivary gland with size variations depending on their location in the salivary ductal system [12]. Others propose that secretory inactivity is a factor leading to the accumulation of sialomicroliths, with obstructive atrophy, inflammation, and compression of the surrounding parenchyma resulting in stagnation of saliva excretion, thus creating an environment for calcium deposition on phospholipid membranes and creating a sialolith [11]. A recent study observed that the induction of an inflammatory reaction can cause an influx of neutrophils into the salivary duct. The activation of these cells can form neutrophil extracellular traps (NETs), which are potent attractors of calcium-based crystals (hydroxyapatite, brushite, and whitlockite), and promote the pathogenesis of sialolithiasis [13]. The possible mechanism of sialolith formation is illustrated in figure 1. Although many efforts have been made to explain the exact pathogenesis of sialoliths, the comparative analysis between sialolith, tonsilloliths and antroliths have not been studied.

Generally, sialoliths are composed of biphasic materials of organic and inorganic matrices, with a central core, a lamellar peripheral structure, and a major component of calcium phosphate [1, 14]. The inorganic phase of the sialolith is mainly composed of carbonate hydroxyapatite whitlockite or calcium carbonate, while the organic phase is mostly composed of cellular debris, mucus, bacteria,

glycoproteins, lipids, and polysaccharides [9]. Sialoliths are mainly composed of elements such as calcium and phosphorus, with small amounts of magnesium, sodium, chloride, silicon, iron, and potassium. There are individual differences in the composition, structure and process of mineralization. There is scarce evidence in the literature about the specific mechanism of lithogenesis, indicating a greater need for further research. Because there is a lack of in vitro and in vivo studies that stimulate sialolith formation, many theories had been proposed and all of these theories could possibly hold some truth. Therefore, it is of great importance to further understand the mechanism of sialolith formation to develop preventative and treatment methods for sialolithiasis.

Tonsilloliths are calcifications that form in the crypts of the palatal tonsils and are responsible for chronic infection. Tonsilloliths demonstrate similar architecture and physiological behavior to dental biofilms. Tonsilloliths are concentrations of aerobic and anaerobic bacteria that calcify over time from a soft gel to a "stone". An oxygen-poor environment is detected at the tonsillolith center with the depletion of surface sugar [15, 16]. An adult palatine tonsil contains approximately 10-20 crypts which become an anaerobic environment in which certain bacteria can accumulate and form biofilms. There have been no ultrastructural and elemental analyses of tonsilloliths. The possible mechanism based in the literature and the current findings is shown in figure 2. In the literature, there are no ultrastructural and elemental analysis of tonsilloliths.

Antroliths are described as calcified masses and deposited calcium salts that form though the retention of inflammatory exudates within the sinus cavity. Although a number of predisposing factors have been identified, such as chronic

inflammation, odontogenic infection, poor sinus drainage, and the presence of foreign bodies in the sinus, the exact pathogenesis of antrolith formation has not been fully elucidated [17]. The foreign body at the core of the antrolith, such as tooth or bone fragments, blood, pus, mucus, or fungi, is usually of endogenous origin [18]. A possible mechanism for anthrolith formation is shown in figure 3.

Previously, several studies have reported on the characterization of pathological deposits such as urinary stones, gallstones and cardiovascular calcification (angioliths) in the human body [9]. Most of the studies on structural characterization of sialoliths include Raman microspectroscopy, thermal analysis, matrix-assisted laser desorption/ionization – mass spectrometry, SX-ray diffraction, X-ray photoelectron spectroscopy, and FTIR spectroscopy [10, 19-21]. However, there are no data or knowledge about the ultrastructural and elemental analysis of sialolith in comparison to tonsillolith and antrolith.

I.2. Sialolithiasis

Sialolithiasis is a common disease of salivary glands characterized by the obstruction of the salivary secretion by a calculus. This is associated with pain and inflammation, and on some occasions with an infection of the affected gland. This disease is considered to be one of the primary causes of chronic obstructive sialadenitis, with a reported prevalence of 1.2% in postmortem studies and an incidence of 2.9-5.5 cases per 100,000 of the population [12]. The submandibular gland is most prone for sialolith formation due to its seromucous saliva content and for its long and curved Wharton's duct. The parotid gland is the second most affected gland followed by the sublingual gland [22]. The diagnosis is based on the medical history, clinical findings,

4

physical examination and imaging techniques. Recurrent pain, swelling of the salivary gland during meals are the most common symptoms of sialolithiasis. Ultrasound and computed tomography are other techniques that are used for detection of sialolith [23].

The clinical concerns of sialolithiasis and its effects on quality of life and morbidity mandate continued efforts for improving treatment methods and strategies. Although several factors predisposing to sialolith formation are known, the cause is still not clear. Therefore, there is no specific effective method to prevent sialolith formation. For treatment, conservative methods have poor effects and are only used in cases of small sialoliths (<4mm) [24]. Recently, sialoendoscopy has been recognized as a new and effective treatment method, but it has its limitations due to the invasiveness associated with the large diameter of the endoscope and is dependent on the surgeon's skill. Complications such as possible minor ductal tears and avulsion of the duct have been reported.

The most recent treatment protocol for sialolithiasis are based in the anatomical location, the size and the accessibility of the sialoliths depending on the type of salivary gland, whether the sialolith is located (1) in the papilla, distal and middle duct, (2) in the proximal to hilar duct system, (3) in the parenchyma [25]. With the development of minimally invasive treatment approaches for sialolithiasis, including intraductal shock-wave lithotripsy, sialendoscopy-assisted transoral duct surgery and the refined retropapillary approach for distal parotid sialolithiasis, it has replaced more invasive treatment approaches such as extracorporeal shock-wave lithotripsy and the combined transcutaneous–sialendoscopic approach [26]. These current minimally invasive treatment methods are effective but not the fastest

method of treatment and require increased efforts. 10-20% of salivary stones are located in the parenchyma, in which they are not primarily accessible with the transoral duct surgery, interventional sialoendoscopy, or with the combined approach, so that extracorporeal shock-wave lithotripsy remains as the only available treatment method. However, the lithotripsy method for sialolithiasis has success rate lower than that of renal stone treatment which is essentially calcium stone [27]. The underlying reason for this fact is still yet unexplained and requires further investigation. Furthermore, 5-15% of sialoliths could not be successfully treated by any other treatment methods. In fact, sialolithiasis still remain to be the main reason for salivary gland resection [28, 29]. The surgical resection of salivary gland is associated with unfavorable cosmetic aspects, reduced saliva production, collateral damage to the lingual nerve and the facial nerve, and the development of Frey's syndrome [25]. Therefore, there is a great demand for research and development of a reliable treatment method for sialolithiasis without morbidity and sequelae to the patients. At the time of writing this manuscript, and to the authors' knowledge, there are no reporting of the ultrastructural and elemental analysis of sialolith in comparison to tonsillolith and antrolith.

The purpose of this study was to investigate the lithogenesis of sialoliths compared to that of other calcifications found in the head and neck region, tonsilloliths and antroliths. The null hypothesis of this study would be that sialolith, tonsillolith and antrolith have no difference in ultrastructure and chemical composition. The determination of the ultrastructure and chemical composition of the sialolith in comparison to tonsillolith, and antrolith is an essential step for the development and application of specific prophylactic and treatment measures.

II. Materials and Methods

II.1. Sialolith, tonsillolith and antrolith specimen collection

We analyzed sialolith, tonsillolith, and antrolith specimen retrieved in the Department of Oral Maxillofacial Surgery of Seoul National University School of Dentistry. This study and its access of patient records were ethically approved by the Seoul National University Institutional Review Board (S-D20220023). The sialoliths were obtained via sialolithotomy, sialendoscopy, direct extraction, or spontaneous extrusion. Specimens were collected from January 2017 to July 2022 and preserved without fixation, fixation in 10% buffered formalin, and fixation in 2.5% glutaraldehyde (GA) solution as routine work for further study. The specimen was screened, and only well-preserved and intact stone samples qualified for further experimentation.

After specimen screening, the patient record was reviewed to identify patients that fulfilled these criteria:

1. Patients with various pathologies treated with sialolith, tonsillolith and antrolith removal. These pathologies included sialolithiasis, tonsillitis, and chronic maxillary sinusitis.

2. Patients with available clinical and radiogram data for all treatment periods and follow-up.

Patients with lacking data such as radiograms and lost during the follow-up period were excluded from this study.

Twenty-five specimens from 23 eligible patients (ten males, 13 females; mean age 37.82 years, ranging from seven to 68 years) were included. These were from patients with chronic sialadenitis with pain and swelling in the submandibular and parotid gland region, recurrent sore throat and odynophagia due to tonsilloliths, and chronic odontogenic maxillary sinusitis.

II.2. Specimen selection and grouping

The calcified stone samples were classified into one of three groups according to the type of specimen

Group A: Sialolith (n=22)

Group B: Tonsillolith (n=1)

Group C: Antrolith (n=2).

II.3. Micro-CT analysis

All specimens were subjected to high-resolution micro-CT scanning using a Skyscan 1273® (Bruker, Kontich, Belgium) with a 0.3 mm copper filter, 136 μA source current, 110 kV source voltage, and 18 μm resolution. The specimens were rotated over 360° with 0.3° steps for each X-ray image. The specimen was mounted in gauge with radiolucent PBS (phosphate buffered saline) sheath buffer. To evaluate the average attenuation, calibration rod pairs composed of epoxy resin embedded with fine CaHA powder at concentrations of 0.25 and 0.75 $g/cm^{3,}$ and at a diameter of 8 mm were used as phantoms.

The micro-CT raw dataset was reconstructed by the NRecon® 1.7.5.1 (Skyscan, Belgium) with a ring artifact correction of 3 and beam hardening correction of 20%. Volumetric visualization was achieved with DataView (Skyscan, Belgium) software. This resulted in images that were 1536 pixels in width and height. Micro-CT can provide a 3D visualization of the inner micro-structures as indicated by changes in the X-ray attenuation value of the specimen [30].

II.4. Histopathological analysis

The tissue sections for light microscope examination were prepared in three steps: dehydration, clearing, and impregnation. Dehydration was carried out in ascending concentrations of ethanol (EtOH): 70% (EtOH) -> 80% (EtOH) -> 90% (EtOH)-> 95 (EtOH) ->100% (EtOH). The clearing consisted of the removal of the dehydrant with Neo-clear® (Aruimea, Madrid, Spain) in this order: 100% (Neo-clear) -> 100% (Neo-clear)-> 100% (Neo-clear)-> 100% (paraffin) -> 100% (paraffin). The histologic slide was stained with H&E. The paraffin-embedded tissue blocks were cut in serial sections of 5 µm, which were then stained with hematoxylin-eosin (H&E). The slides were then scanned with a 3D scanner (PANNORAMIC 250 Flash III; 3DHISTECH, Budapest, Hungary) and examined using slide-viewing software (CaseViewer version 2.0; 3DHISTECH, Budapest, Hungary).

II.5. Sialolith, tonsillolith and antrolith analysis by SEM

The specimen was immediately placed in a 2.5% glutaraldehyde solution for fixation. Before electron microscopic examination, the specimens were partially encapsulated in a heavy putty impression material and sectioned through their median region

without damaging the layered structure. The specimen was removed from the putty impression material and half of the specimen was used for SEM examination, and the remainder was used for histology and TEM examination.

As the specimen is electrically non-conducting, sputter coating with platinum (Pt) was carried out to increase the signal-to-noise ratio and prevent charging of the specimen. This would otherwise occur because of the accumulation of static electric fields before SEM examination (Apreo S®, Thermo Fisher Scientific, Waltham, MA, USA). The secondary electron (SE) detection mode was used for the ultrastructural surface analysis, while the backscattered electron (BSE) detection mode was used to analyze the different phases and compositions based on the differences in atomic number. We examined the samples from the periphery to the core of the specimen with nine to 15 focal points. The surface of the cross-section was thoroughly examined under 500× magnification and areas with representative features were chosen for micrographic and elemental analysis. The SEM was operated at 10 kV; and 65×, 500×, 1000×, 2500×, 5000×, 10,000×, and 20,000× micrographs were acquired.

II.6. Chemical composition analysis by EDS

The element composition of the specimens was accessed by using an EDS instrument (XFlash® 6, Bruker, Berlin, Germany) connected to a microscope detector and the ESPRIT® analysis software (Bruker, Berlin, Germany). Regions of interest (ROIs) for EDS element analysis were derived from the center, middle, and external surface of each specimen from each group. The representative region was chosen and analyzed under a magnification of 10,000×.

The EDS method involved qualitative and semi-quantitative microanalysis, including element distribution mapping. The representative point of each region was chosen and analyzed under a magnification of 10,000×. The mass concentration (C) was classified by the percentage of weight (wt%) and atomic weight (at%).

II.7. TEM experiment

Specimen preparation involved fixation of samples in 2.5% glutaraldehyde for at least three days. For the TEM examination (JEM-1400 Flash®, Jeol Ltd., Tokyo, Japan), the specimen was stripped into a 1×1×1 mm block, embedded in epoxy resin, and cut into ultrathin sections (70-80 nm). Sections of 1 μm were stained with toluidine blue (TB) and examined under microscope (BX41 Light Microscope®, Olympus Co., Tokyo, Japan).

TEM (JEM-1400 Flash®, Jeol Ltd.) was used to observe the components present in the specimen with 3,000×, 6,000×, 10,000× magnifications.

II.8. Statistical analysis

For the chemical composition analysis by EDS, the means and standard deviations (SDs) of the wt% and at% were calculated. The data normal distribution was tested by Shapiro–Wilk test. The differences were tested by one-way ANOVA. Statistical analyses were carried out using SPSS version 25.0 (IBM Corp., Armonk, NY, USA). $P < 0.05$ was considered statistically significant.

III. Results

III.1. Patient characteristic and demographic data

Twenty-three patients with a total of twenty-five specimens were eligible for the study after the inclusion and the exclusion criteria. The patient and treatment data are presented in Table 1. The average age was 37.92±15.89, ranging from 7 to 68 years old. There were 10 (43.48%) male patients and 13 (56.52%) female patients with a gender ratio of 0.77:1.

III 2. The sialolith, tonsillolith and antrolith specimen data

The anatomical sites in which the specimen was located are presented in Table 1. In 19 patients (95%) out of 20 patients in group A, the sialoliths were located in the submandibular salivary gland. Out of 22 sialolith specimens, ten cases presented on the left submandibular salivary gland (45.45%), while eight cases presented on the right side (36.36%) and three cases on both sides of the submandibular salivary glands (13.63%). Only one case presented a sialolith on the left parotid salivary gland (4.24%). Regarding their number of occurrences, single stones were found in 15 cases (75%), two stones in three cases (15%), while two cases had more than two sialoliths (10%). The two group B tonsilloliths presented on the right tonsils, and two group C antrolith specimens were obtained from the right and left maxillary sinuses.

III.3. Micro-CT analysis sialolith, tonsillolith and antrolith

The micro-CT scanning allowed 3D visualization of the specimen in groups A, B, and C (Figs. 4-6). The sialolith specimens showed an onion skin-like layered structure with alternating radiodense (highly mineralized) and radiolucent (organic) layers in both submandibular and parotid gland sialoliths. In group A, 11 sialolith specimens had a single core (A4, A5, A8, A9, A12, A15, A-16-1, A16-2, A18, A19, A20), while one sialolith had multiple cores (A7), one sialolith had two cores (A11), and one sialolith had no distinct core (A10). The sialolith cores in group A displayed either distinctively higher or lower degrees of mineralization compared to the surrounding layers as inferred from the brighter and darker contrast in the radiographic data. The sialoliths had nearly spherical (A4, A8, A16-1, A19, A20), oval (A5, A15, A16-2), or asymmetrical (A7, A11, A18) shapes. Apart from the shapes, there were concentric growth patterns (A4, A5, A15, A19) and irregular ones (A7, A8, A9, A11, A16-1, A16-2, A18, A20). However, in many situations, variation between these two types of growth patterns was observed.

Group B tonsillolith showed a homogeneous structure without a concentric laminated pattern (B1). The specimen showed a higher degree of homogeneous mineralized structure compared to that of group A. The group C specimen revealed a compact homogeneous structure (C2) that had more internal voids (C1) compared to that of group A and group B. 3D reconstructed images of the specimen are shown in figures 4-6. Table 2 shows the morphometric parameters of groups A, B, and C.

III.4. Histopathological findings

4.1 Histological findings in group A

In general, all of the sialolith specimens showed concentric lamellar structures with organic and inorganic substances. Eosinophilic characteristics were found at the core. A laminated pattern of a teardrop-shaped globular structure was seen at the periphery. A laminated concentric pattern of the basophilic zone indicating a highly mineralized area of the stone which is mostly composed of inorganic material. Small amounts of bacteria were located at the outer shell of the sialolith containing salivary ductal epithelium (Figs. 7-13).

4.2 Histological findings in group B

The tonsillolith specimen of a 53-year-old male patient stained with hematoxylin-eosin (H&E) demonstrated a mature stage of development; this tonsillolith was surrounded by fibrinous debris and inflammatory cells (Figs. 14A-B). The tonsillolith revealed degrees of immature calcification of organic and inorganic materials. A duct-like structure was observed at the center of squamous epithelium indicative of the minor salivary gland duct (Fig. 14C). Squamous epithelium on the surface of the tonsillolith was noted to extend toward the lining of the tonsillar crypt (Figs. 14D-F). At high magnifications, the tonsillolith was composed of a dense matrix, and microbial colonies composed of rods and cocci were observed (Figs.14G-I).

4.3 Histological findings in group C

The lesion was not encapsulated and showed a homogeneous lamellar bone with fibrous marrow cavities. The woven bone was replaced by lamellar bone with Haversian canals at the periphery (Figs. 15A-D). The lamellae of this bone were organized longitudinally in well-differentiated and interlacing trabeculae, characteristic of mature cancellous bone. The osteocytes were randomly and unevenly distributed with spindle-shaped lacunae. Cellular elements included abundant eosinophilic and finely granular cytoplasm, eccentrically placed oval nuclei, and absent nucleoli. Characteristics of neoplastic bone, such as thickened trabeculae or architectural atypia, were absent. The attached soft tissue showed inflamed granulation tissue with bone sequestrum and mainly consisted of diffuse inflammatory cells including macrophages, lymphocytes, and plasma cells (Figs. 15E-H).

III.5. SEM findings of sialolith, tonsillolith and antrolith

5.1. Ultrastructural findings in group A

The general architecture in SEM findings revealed a concentric lamellar structure with alternating mineralized and organic material (Figs. 16A-C). The detailed structure of each alternating layer is analyzed in the following sialoliths at 1,000× and 20,000× magnifications.

Sialolith A5 showed a layered structure with a single core. Irregular structure seen at the periphery of the sialolith at point 01. A plate-like structure was observed on the point 02. Extracellular exosomes that form a tridimensional globular structure were seen at point 03 at the center of the sialolith (Fig. 17).

Sialolith A6-2, obtained from the submandibular salivary gland, shows a layered structure (Fig. 18). At the very outer layer of the sialolith, a long rod-shaped bacterial biofilm cave (yellow arrowheads) is seen with calcium nanoparticles on point 01. The SEM image shows the layered structure of the sialolith (white lines). At the intermediate layers on points 02, 03, and 04, dense hydroxyapatite aggregates are observed with bacterial empty casts (blue arrowheads) at 20,000 × magnification. Point 05 shows a more porous structure than points 02, 03, and 04, but rudely hexagonal, fibrous, irregularly shaped hydroxyapatite crystals are observed. Fibrous and irregularly shaped hydroxyapatite crystals show random orientation from point 05. Point 06 shows the irregularly shaped hydroxyapatite occurring in cluster masses or individual crystals (black arrowheads). Points 07, 09, and 11 show a coarser structure of hydroxyapatite crystal aggregation. Points 08 and 14 depict a densely aggregated layer of microscopic mineral masses compatible with octacalcuim

17

phosphate. A filament pattern of the inorganic matter compatible with carbonate apatite arranged in different orientations was observed on point 10 (red arrowheads). Calcite-like crystals are seen on point 13 (blue arrowheads). The irregular structure shows platy, rudely hexagonal and irregularly shaped hydroxyapatite crystals in random orientations (F, blue arrows).

The heterogeneous layered sialolith A14 from the submandibular salivary gland shows a single core with a loose layer of granule-shaped crystals with long rod-shaped bacteria at the peripheral layer on point 01 with 20,000 × magnification. At the middle layer, denser microbial product or biofilm was observed on point 02. Points 03, 04, 07 and 08 at the surface of the core show mineral masses compatible with octacalcium phosphate. At the core of the sialolith a hexahedral calcite crystal having a mineral composition compatible with whitlockite (blue arrowhead) is observed in a long rod-shaped bacterial mold on point 05. At the core of the sialolith, less dense hydroxyapatite aggregates are observed on point 06 (Fig. 19).

A recurrent sialolith (A17) from the left submandibular salivary gland was analyzed at the cross-section surface at the center with 13 points of interest. The outer surface of the stone shows a calcified irregular fibrous structure with a lacy pattern (white arrow) from point 01 at 20,000× magnification. Hexagonal and irregularly shaped hydroxyapatite occurring in clusters or as crystals are shown at point 02. Alternating layers of coarse and dense aggregates of hydroxyapatite crystals are seen on points 03, 04, 05, and 07. Globular patterns of cores and surrounding concentric laminated structure are observed at points 06 and 09 (yellow

arrowheads). A diatomite particle is found at point 08 at 10,000× magnification (blue arrowheads). Irregularly shaped filamentary crystals are seen at point 12 (Fig. 20).

BSE mode analysis of the recurrent sialolith (A17) showed the concentric pattern of mineralization at 500× and 10,000× magnifications. BSE mode allowed comparison of the different chemical composition in each layer as the probability of electron backscatter is proportional to the atomic mass of the specimen element (Fig. 21). The fine structure of each layer was threaded with varying sizes and degrees of mineralized globules. The globules had different sizes measuring up to 6 μm. The core of the sialolith consisted of a less mineralized mass at point 04. The surrounding outer layer consisted of darker and less mineralized structure. The thickness of each layer decreased from the outer layer at the periphery to the core of the sialolith.

5.2. Ultrastructural findings in group B

Compared to the ultrastructural findings of group A, the group B specimen did not present with concentric laminated structures. The SEM analysis of the tonsillolith showed hexahedral-shaped crystals on all points of interest (Fig. 16E, 22). The outer layer of the tonsillolith showed a filamentous structure that suggested bacterial accumulation on point 10.

Ultrastructural findings in group C

The general structure of group C showed a homogeneous structure without concentric laminated mineral deposits. The antrolith (C1) specimen from group C was analyzed at the cross-sectional surface with 14 focal points of interest. Non-crystalline and smooth surfaces were found in the peripheral and central area of the

19

specimen at points 01-11. Coarse crystalline micro aggregates were identified in the core regions (Figs. 16F-G, 23-24).

III.6. Chemical composition of sialolith, tonsillolith and antrolith

6.1. EDS analysis of specimen in groups A, B, and C

The chemical composition of the specimen was analyzed and recorded at the peripheral (P), middle (M), and core (C) layers. The compositional analysis of each specimen consistently demonstrated a high fraction of calcium (Ca), carbon (C), oxygen (O), and phosphate (P) in group A, B, and C (Table 3). However, the level of each element varied in each group. The wt% and at% of Ca in group A were higher (20.72 ± 5.53 wt% and 9.55 ± 2.77 at%) compared to group B (17.48 ± 3.02 wt% and 8.23 ± 1.51 at%), and group C (17.18 ± 6.98 wt% and 7.28 ± 3.31). The differences were not, however, significantly different (Table 3). The C level wt% and at% were significantly higher in group C (32.86 ± 17.60 wt% and 43.23 ± 17.25 at%) compared to those of group A (21.36 ± 4.50 wt% and 31.85 ± 5.29 at%) and group B (15.33 ± 4.50 wt% and 23.92 ± 6.40 at%) (p = 0.006; p = 0.004, respectively). The wt% and at% of O was significantly higher in group B (38.31 ± 2.70 wt% and 45.95 ± 3.46 at%), compared to those of group C (29.24 ± 3.31 wt% and 30.52 ± 4.33 at%) (p = 0.016; p = 0.002, respectively). The wt% and at% Ca/P ratios were 1.19 ± 0.85, 2.20 ± 2.33 respectively in group A; group B showed a wt% of 1.27 ± 0.62 and at% of 0.97 ± 0.48; and group C showed a wt% of 3.59 ± 1.54 and at% of 2.77 ± 1.34.

The comparative chemical composition analysis between the groups are shown in Table 4. Excluding the major three elements that constituted the sialolith (Figs. 25-28), tonsillolith (Fig. 29) and antrolith (Figs. 30-31), many other elements were detected. These elements included fluorine (F), nitrogen (N), sodium (Na), silicon (Si), and magnesium (Mg); these were detected in all groups. Other elements such as copper (Cu) and zinc (Zn) were found only in group A; groups B and C

showed no trace of these. Traces of iron (Fe) were found only in group B, while zirconium (Zr) was found in both groups A and B. Wt% of N in group A was significantly higher (14.68 ± 5.63 wt%) compared to that in groups B and C (p = 0.031).

6.2. Comparison of elemental analysis at the peripheral, middle and core regions in group A

For the EDS analysis, more traces of chemical elements were found in the peripheral layer of the sialolith compared to the middle and core layers. Ca, C, O and P were the major elements found in all hydroxyapatite layers of the sialolith. Elements such as Ca, C, O, N, Na, P, Si and Mg were found in more than two regions. Traces of Cu (wt% 13.39±0.00 and at% 4.62±0.00) and Zn (wt% 10.68±0.00 and at% 3.59±0.00) were found only in the peripheral region of the sialolith (Table 5). Traces of F were found in the periphery and the middle layer of the sialolith but were absent in the core layer. Wt% and at% of Mg were highest in the inner core layer of the specimen (wt % 10.72±7.38 and at% 6.78±4.34) but were not significantly different.

The peripheral layer of group A showed major elements including Ca, C, O, N, Na, P, Si, and Mg. Other elements such as Cu, F, Zn, and Zr were also found. The core of the sialoliths was mostly composed of Ca, C, O, N, Na, P, Si, and Mg.

The EDS mapping showed homologous elemental distribution in sialoliths (Figs. 26-28), except in sialolith A5, where a non-homologous elemental distribution of Si and Ca was found in the middle layer (02-M) (Fig.25).

6.3. Comparison of elemental analysis at the peripheral, middle and core regions in group B

The EDS results of the tonsillolith specimen analyzed at the peripheral, middle and core regions are presented in Table 6. The EDS mapping showed homologous elemental distribution in the tonsillolith (Fig. 29). The peripheral layer of the tonsillolith showed major elements found in groups A and C, including Ca, C, O, N, Na, P, Si, and Mg. However, a trace of Fe was found only on the outer layer of group B. The inner layer was mostly composed of Ca, C, O, N, Na, P, Si, and Mg. In the core, traces of F and Zr were found in group B.

6.4. Comparison of elemental analysis at the peripheral, middle and core regions in group C

The EDS results of the antrolith specimen analyzed at the peripheral, middle and core regions are presented in Table 7. Major elements found in sialoliths and tonsilloliths were also found in the peripheral, middle, and core layer of group C. These elements included Ca, C, O, F, N, Na, P, Si, and Mg (Figs. 30-31).

III.7. TEM analysis

For the TEM analysis, highly mineralized/crystalline regions appear dark in the bright field imaging due to staining and/or the diffraction of heavy elements (Figs.32-35). In submandibular salivary gland sialoliths A6-1, globular structures with a double membrane were detected undergoing intra-vesicular calcification (Figs. 32A-B). Lipid vesicles and finger-like globular structures were also detected (Figs. 32C-H). The layered appearance of the sialolith showing the globular mineralized

structure in the external lamella with a heterogeneous crystalline needle-like pattern was observed (Figs. 33A-B). Large single crystals and deposition of inorganic material at the inner lamellae were observed in darker contrast compared to the surrounding structure (Figs. 33E-F). Needle-like filamentary crystals suggested hydroxyapatite structure (Figs. 33G-H).

Two types of calcification were found in pediatric sialolith A13, intra-vesicular and extra-vesicular deposition of inorganic matter and large membranous bodies (Figs. 34A-D). The globular structure was noticed to have an internal and surface opaque contraction. Some globular structures had double membranes. Extra-vesicular deposition of inorganic matter (Figs. 34E-H).

In the peripheral lamella, a homogenous layer of organic compounds was found in recurrent sialolith A17. Hydroxyapatite crystal aggregates were found within the globules and at the outer edges of the globules (Figs. 35A-C). Deposition of large single microcrystalline inorganic compounds, such as needle-like filamentary crystals, was arranged in clusters and different directions and clusters of parallelepiped crystals were observed (Figs. 35E-H).

The B1 tonsillolith had stratified squamous epithelium in its peripheral area (Figs 36A-B). Bacteria were present in the middle layer of the tonsillolith (Figs. 36C-D). Needle-like crystals in the core region and extra-vesicular deposition of inorganic material were also observed (Figs. 36E-H). In the outer layer of the C2 antrolith, an osteoblastic rimming was observed (Figs. 37A-B). The middle region of the specimen was mainly composed of dense, mature, and predominantly lamellar

bone (Figs. 37C-D). The core region had no Haversian canals and fibrous component

(Figs. 37E-H).

IV. Discussion

Physiological mineralization is limited to specific sites in the skeletal tissues, including the growth plate cartilages, bone, and teeth. Uncontrolled and pathological mineralization may occur in any soft tissue within the human body [31]. In particular, the calcifications in the articular cartilage, cardiovascular tissues, and kidneys are studied extensively. However, there are limited data on the ultrastructural and elemental analysis of calcifications in the head and neck region, including sialoliths, tonsilloliths and antroliths.

The pathogenic mechanism of sialolith formation could be explained by four main mechanisms:

1. Bacteria-associated sialolithiasis

2. Protein coagulation by different cross-linking enzymes in saliva

3. Salivary exfoliated cells-associated sialolithiasis

4. Others including trauma, salivary duct obstruction, habit, systemic metabolism, etc.

Biofilms are a community of microorganisms that live encased in an EPS matrix. A study by Kao et al. suggested that biofilms and their interactions with host immune cells and calcium nanoparticles form the nidus for calcium crystal deposition [32]. Biofilms have also been shown to accumulate calcium. Calcium is essential for the cross-linking of alginate in the EPS. Calcium nanoparticles of 500 nm that produce calcium apatite from calcium and phosphorus at normal physiological conditions. The interaction of calcium nanoparticles, host cells, and biofilm may serve as a strong scaffold for further calcium deposition and sialolith

formation. The main strain of bacterial organisms found in the sialoliths are *Bacillus Subtilis, Streptococcus mitis/oralis, Sterptococcus angionosus, Rothia spp.. Streptococcus constellatus, Streptococcus gordonii, Staphylococcus aureus* and coagulase-negative *Staphylococcus epidermidis* [33, 34]. In a previous proteomics study of sialoliths, a group of proteins that defend against different types of external pathogens were identified: lactoperoxidase (LPO), histatin (HTN1), lysozyme (LYZ), and cationic antimicrobial peptide (CAMP) [35].

In our ultrastructural study with SEM and TEM analysis, we found structures resembling extracellular exosomes that form a tridimensional globular structure. They are thought to be carriers of transporters of proteins from the immunologic and metabolic processes and their regulators. They are a constitutive part of the extracellular matrix and apparently a site for deposition of amorphic mineral microcrystals. Previous study by Busso et al. found significant values of immune indicators from the biological processes domains such as immune system processes and immune and defense responses, which were the integral part of the extracellular matrix. These proteins may be deposited in salivary stones during stone growth, and therefore, could have multiple exosomal origins [36]. These findings suggest the important role of immune response in the process of sialolith formation.

Amongst the proteins that are present in the sialolith, the following calcium binding proteins have a major role in balancing minerals and prevent spontaneous crystallization in the salivary gland and oral cavity: statherin (STATH), histatin (HTN1), calmodulin-like protein 5 (CALML5), basic salivary proline-rich protein 1 (PRB1), proline rich protein HaeIII subfamily 2 (PRH2) [35]. STATH has an important role in the saliva which inhibit spontaneous precipitation of calcium and

phosphate salts from the saliva [37]. HTN1 is a histidine-rich peptide that is present in saliva and have anti-inflammation, detoxification, and remineralization effects. The CALML5 protein is involved in calcium-binding, intracellular signaling and the differentiation of keratinocytes [38]. The PRB1 and PRH2 are acknowledged as the modulators of calcium phosphate chemistry, which are selectively absorbed into the hydroxyapatite, and modulate bacterial colonization [39].These cross-linking enzymes present in sialolith are thought to have a role in the pathogenic mechanism of hydroxyapatite precipitation in the sialolith.

Regarding other actors such as trauma, salivary duct obstruction, habit, and systemic metabolism, etc., ductal trauma is thought to be one of the factors that contribute to sialolith formation. However, based on our experience and the literature review, endoscopic sialolith removal does not result in sialolith formation. Regarding the habit, a previous study found a positive association between sialolithiasis in the a population of ≤40 years-old [40]. And considering the systemic metabolism, sialoliths tends to be unilateral, which argues against a systemic metabolism and suggests local factors to play major roles [32].

A study by Stoodley et al. showed that tonsilloliths exhibit similar structure and chemical gradients to a dental biofilm. This physiological activity was analyzed by confocal microscopy and by microelectrodes that measured aerobic and anaerobic respirations and acid production [16]. In our study we found filamentous bacteria at the peripheral layer of the specimen. The composition of the developing biofilm is determined by several factors such as the site of colonization and the type of the surface [41].

Antroliths are a rare entity and are usually asymptomatic. In most cases, antroliths are discovered incidentally during routine examinations and are thought to have endogenous and exogenous origins [18]. In our literature review, there was a lack of information on ultrastructural and elemental analysis of antroliths. Most of the recent studies focus on case reports and clinical studies using radiographic analysis methods such as cone-beam computed tomography [42]. As the incidence of antroliths are quite rare and there is a lack of research on this field, the pathogenesis of antroliths are not completely understood. In our study, we found that the antroliths had a different structure compared to sialoliths, where they had a concentric laminated structure with a core. The study of the core of lithiasis give valuable information on the generation, precipitation, and aggregation of minerals [43]. The determination of the structural characteristics and the composition of all parts of the stone especially the core is essential for understating the mechanism of stone genesis. In human kidney stones, amorphous calcium phosphate was found to promote the aggregation of amorphous calcium oxalate complexes which induce the nucleation and growth of urinary stones [44]. Although many theories have been stipulated to explain the sialolith formation, many theories focus on the core or nucleus that may initiate the development. Takeda proposed a mechanism in which crystalloid present in a salivary gland may aggregate and form a core that organic and inorganic materials would deposit [45]. On the other hand, we found that antrolith had no core and consist of lamellar bone structure. This bone structure could originate from the surrounding bone of the maxillary sinus wall as a result of pathological conditions involving the sinus.

From the comparative micro-CT, SEM, and TEM analyses among groups A, B, and C, the sialolith, tonsillolith, and antrolith specimens had different micromorphology, suggesting different pathways of formation. In general, the sialoliths mostly had concentric laminated structure, in which the chronological order of development could be analyzed in detail. However, the tonsillolith and antrolith showed homogeneous structures without any layered microstructure. The micro-CT analysis allowed nondestructive imaging of the major core of the sialoliths. These cores are sometimes less mineralized and could be damaged or missed during the specimen preparation process for SEM and TEM [46]. Based on the micro-CT scanning, the cores of each sialolith could be classified as highly mineralized (A5, A20) and less mineralized (A4, A7, A8, A9, A11, A15, A16-1, A16-2, A18, A19) in comparison to the surrounding layers. These findings are confirmed with the histology findings showing a less mineralized core in sialoliths A2 and A14 surrounded by contrasting higher mineralized middle and outer layers. In a previous study, no organic cores were observed in the central part of the sialoliths [47]. The presence of concentric laminated structure threaded with globules could be explained by the Liesegang and Ostwald precipitation mechanism [48, 49]. A combination of micro-CT and ultrastructural analysis with SEM and TEM can be effectively used to characterize the specimen.

During our SEM analysis, we found a tube-shaped diatomite at the core of the recurrent sialolith A17. Diatomite or diatomaceous earth is a naturally occurring mineral resource containing fossilized remains of single-celled alga. These particles have many pores (pore sizes 50–200 nm). The main chemical composition is inorganic polymer-amorphous silica (SiO_2) [50, 51]. Diatomites have size-, shape-,

and dose-dependent cytotoxicity [51]. In the literature review, there were no reports of diatomite in the core of the sialolith. Diatomites are extensively used as two grades, food-grade for internal use for humans, and non-food-grade used in industrial practices. Recently, topical and oral use of diatoms have become more common, due to various health benefits claims that are unsupported by scientific evidence. One of the main sources of diatomite consumption is a toothpaste. Diatomite originated from an alginate impression material has been reported to cause foreign-body mucosal granuloma [52]. Although, only one case showed a diatomite at the core of the sialolith, it could be assumed that diatomite originating from a toothpaste could have retrograde migration into the salivary secretion duct.

The main elements of sialoliths have been reported to be Ca, P and O. A study using Fourier transform infrared (FTIR), FT-Raman, and fluorescence spectroscopic techniques showed the ratio of the major elements Ca and P to be 7:3[53]. In another study using X-ray microanalysis, the component elements of sialoliths were Ca, O, S, and Na. The Ca and P ratio was calculated to be 1.60-1.89 [54, 55]. The chemical constitution of each specimen varied from one to another. In our study, we found elements Ca, C, O, F, N, Na, P, Si, and Mg in sialoliths, tonsilloliths, and antroliths. In addition, only sialoliths had elements such as Cu, Zn, and Zr, while tonsilloliths had traces of Fe. The main inorganic components of sialoliths are reported to be apatite ($Ca_{10}(PO_4)_6(OH)_2$), whitlockite ($Ca_3(PO_4)_2$), and brushite ($CaHPO_4$ $2H_2O$). Other components include weddellite and octacalcium phase.

Other human liths such as the renal and kidney stones has been studied extensively due to their symptomatic nature, such as pain, infection and obstruction,

which can affect patient's quality-of-life. In fact, acute passage of kidney stones is the ninth most common cause for emergency visit [56]. Sialoliths on the other hand are generally asymptomatic in nature [57]. The mechanism/pathophysiology of kidney stones formation has been established and preventative method along with minimally invasive treatment methods, such as dissolution therapy of kidney stones were developed [2]. In some cases, depending on the size, location and the accessibility of the sialolith, extirpation of the salivary gland may be performed, where the sialolith is located in the parenchyma of the salivary gland or the proximal part of the duct. Similarly, the dissolution of the sialolith located in a difficult location for minimally invasive method, would be a desirable method over the extensive extirpation of the whole salivary gland. Therefore, understating the sialolith growth requires knowledge on the sialolith chemical composition, crystalline microstructure and the biomolecules derived from the host and the resident bacteria. In the current study, the main chemical composition of sialoliths were Ca, C, O and P, which were found in all layers. In the process of sialolith formation, the interaction of calcium nanoparticles, salivary exfoliated host cells, bacterial biofilm, and protein coagulation by different cross-linking enzymes in saliva are important factors that need to be corrected. The goal, therefore would be to reduce the risk of precipitation or aggregation of calcium nanoparticles in the lithogenesis of sialoliths.

V. Conclusion

This was a new comparative, ultrastructural and elemental study between different types of calcifications found in the Oral and Maxillofacial Surgery field. The study demonstrated that sialoliths, tonsilloliths and antroliths had completely different micromorphology and different elemental composition using micro-CT, SEM, EDS, and TEM analysis.

The main pathogenic mechanism of sialolith formation could be explained by four main mechanisms:

1. Bacteria-associated sialolithiasis

2. Protein coagulation by different cross-linking enzymes in saliva

3. Salivary exfoliated cells-associated sialolithiasis

4. Others including trauma, salivary duct obstruction, habit, systemic metabolism, etc.

The main elemental composition of sialoliths were O, C, Ca, N, Cu, P, Zn, Si, Zr, F, Na, and Mg. The peripheral layer had an expanded elemental composition that included Cu, Zn and Zr compared to that of the middle and core regions, while the middle layer had a small amount of F. In tonsilloliths, a small amount of Fe was found in the peripheral region. The antroliths had a shorter component list: Ca, C, O, F, N, Na, P, Si, and Mg.

The sialolith had a concentric laminated structure with highly mineralized or less mineralized core, while tonsillolith and antrolith lacked a core. Antrolith showed a structure and composition similar to that of lamellar bone. The distinguishing ultrastructural characteristics can be used in lithogenesis studies.

Further progress in developing a desirable treatment or preventative method for sialolithiasis would be the dissolution of the sialolith depending on the size, location and the accessibility, as well as reducing the risk of precipitation or aggregation of calcium nanoparticles in the lithogenesis of sialolith. This study's clinical implication is the undertaking of the first step in developing future intervention and treatment methods.

References

1.   Kodaka T, Debari K, Sano T, Yamada M. Scanning electron microscopy and energy-dispersive X-ray microanalysis studies of several human calculi containing calcium phosphate crystals. Scanning Microscopy. 1994;8(2):10.

2.   Khan SR, Pearle MS, Robertson WG, Gambaro G, Canales BK, Doizi S, et al. Kidney stones. Nat Rev Dis Primers. 2016;2(1):16008.

3.   Matsuura K, Maehara N, Hirota A, Eguchi A, Yasuda K, Taniguchi K, et al. Two independent modes of kidney stone suppression achieved by AIM/CD5L and KIM-1. Commun Biol. 2022;5(1):783.

4.   Sivaguru M, Saw JJ, Williams JC, Lieske JC, Krambeck AE, Romero MF, et al. Geobiology reveals how human kidney stones dissolve in vivo. Sci Rep. 2018;8(1):13731.

5.   Miller AW, Penniston KL, Fitzpatrick K, Agudelo J, Tasian G, Lange D. Mechanisms of the intestinal and urinary microbiome in kidney stone disease. Nat Rev Urol. 2022;19(12):695-707.

6.   Zarse CA, McAteer JA, Sommer AJ, Kim SC, Hatt EK, Lingeman JE, et al. Nondestructive analysis of urinary calculi using micro computed tomography. BMC Urol. 2004;4(1):15.

7.   Williams JC, Jr., McAteer JA, Evan AP, Lingeman JE. Micro-computed tomography for analysis of urinary calculi. Urol Res. 2010;38(6):477-84.

8.   Leng S, Huang A, Cardona JM, Duan X, Williams JC, McCollough CH. Dual-energy CT for quantification of urinary stone composition in mixed stones: a phantom study. AJR Am J Roentgenol. 2016;207(2):321-9.

9.   Faklaris I, Bouropoulos N, Vainos NA. Composition and morphological characteristics of sialoliths. Crystal Res Technol. 2013;48(9):632-40.

10.   Szalma J, Böddi K, Lempel E, Sieroslawska AF, Szabó Z, Harfouche R, et al. Proteomic and scanning electron microscopic analysis of submandibular sialoliths. Clin Oral Investig. 2013;17(7):1709-17.

11.   Harrison JD. Causes, natural history, and incidence of salivary stones and obstructions. Otolaryngol Clin North Am. 2009;42(6):927-47.

12.   Sánchez Barrueco A, López-Acevedo Cornejo MV, Alcalá Rueda I, López

Andrés S, González Galán F, Díaz Tapia G, et al. Sialolithiasis: Mineralogical composition, crystalline structure, calculus site, and epidemiological features. Br J Oral Maxillofac Surg. 2022:[Online ahead of print].

13.   Schapher M, Koch M, Weidner D, Scholz M, Wirtz S, Mahajan A, et al. Neutrophil extracellular traps promote the development and growth of human salivary stones. Cells. 2020;9(9).

14.   Rakesh N, Bhoomareddy Kantharaj YD, Agarwal M, Agarwal K. Ultrastructural and elemental analysis of sialoliths and their comparison with nephroliths. J Investig Clin Dent. 2014;5(1):32-7.

15.   Krespi YP, Kizhner V. Laser tonsil cryptolysis: in-office 500 cases review. Am J Otolaryngol. 2013;34(5):420-4.

16.   Stoodley P, Debeer D, Longwell M, Nistico L, Hall-Stoodley L, Wenig B, et al. Tonsillolith: not just a stone but a living biofilm. Otolaryngol Head Neck Surg. 2009;141(3):316-21.

17.   Chen HH, Yi CA, Chen YC, Tsai CC, Lin PY, Huang HH. Influence of maxillary antrolith on the clinical outcome of implants placed simultaneously with osteotome sinus floor elevation: A retrospective radiographic study. Clin Implant Dent Relat Res. 2021;23(6):833-41.

18.   Henriques JC, Kreich EM, Rosa RR, Castilho JC, de Moraes LC, de Moraes ME. Noninvasive aspergillosis as a maxillary antrolith: report of a rare case. Quintessence Int. 2012;43(2):143-6.

19.   Jayasree RS, Gupta AK, Vivek V, Nayar VU. Spectroscopic and thermal analysis of a submandibular sialolith of Wharton's duct resected using Nd:YAG laser. Lasers Med Sci. 2008;23(2):125-31.

20.   Sabot JF, Gustin MP, Delahougue K, Faure F, Machon C, Hartmann DJ. Analytical investigation of salivary calculi, by mid-infrared spectroscopy. Analyst. 2012;137(9):2095-100.

21.   Kinoshita H, Miyoshi N, Miyoshi K, Ogawa T, Ogasawara T, Kitagawa Y, et al. Phosphate and amide III mapping in sialoliths with Raman microspectroscopy. J Raman Spectrosc. 2008;39(3):349-53.

22.   Lommen J, Schorn L, Roth B, Naujoks C, Handschel J, Holtmann H, et al. Sialolithiasis: Retrospective analysis of the effect of an escalating treatment

algorithm on patient-perceived health-related quality of life. Head Face Med. 2021;17(1):8.

23.   Kim DH, Kang JM, Kim SW, Kim S-H, Jung JH, Hwang SH. Utility of ultrasonography for diagnosis of salivary gland sialolithiasis: A meta-analysis. Laryngoscope. 2022;132(9):1785-91.

24.   Tretiakow D, Skorek A, Ryl J, Wysocka J, Darowicki K. Ultrastructural analysis of the submandibular sialoliths: Raman spectroscopy and electron back-scatter studies. Ultrastruct Pathol. 2020;44(2):219-26.

25.   Koch M, Mantsopoulos K, Müller S, Sievert M, Iro H. Treatment of sialolithiasis: What has changed? An update of the treatment algorithms and a review of the literature. J Clin Med. 2021;11(1).

26.   Mantsopoulos K. Treatment of salivary gland diseases: established knowledge, current challenges and new insights. J Clin Med. 2022;11(3).

27.   Escudier MP, Brown JE, Drage NA, McGurk M. Extracorporeal shockwave lithotripsy in the management of salivary calculi. Br J Surg. 2003;90(4):482-5.

28.   Erbek SS, Köycü A, Topal Ö, Erbek HS, Özlüoğlu LN. Submandibular gland surgery: Our clinical experience. Turk Arch Otorhinolaryngol. 2016;54(1):16-20.

29.   Papaspyrou G, Werner JA, Sesterhenn AM. Transcervical extirpation of the submandibular gland: the University of Marburg experience. Eur Arch Otorhinolaryngol. 2014;271(7):2009-12.

30.   Latief FDE, Sari DS, Fitri LA. Applications of micro-CT scanning in medicine and dentistry: Microstructural analyses of a Wistar Rat mandible and a urinary tract stone. J Phys Conf Ser. 2017;884:012042.

31.   Kirsch T. Determinants of pathological mineralization. Curr Opin Rheumatol. 2006;18(2):174-80.

32.   Kao WK, Chole RA, Ogden MA. Evidence of a microbial etiology for sialoliths. Laryngoscope. 2020;130(1):69-74.

33.   Kim YS. Identification of a bacterial strain, Bacillus Subtilis, causative for sialolithiasis and its increased adherence on hydroxyapatite. Kor J Oral Maxillofac Pathol. 2011;35(5):247-53.

34.   Perez-Tanoira R, Aarnisalo A, Haapaniemi A, Saarinen R, Kuusela P, Kinnari TJ. Bacterial biofilm in salivary stones. Eur Arch Otorhinolaryngol.

2019;276(6):1815-22.

35.   Czaplewska P, Bogucka AE, Musiał N, Tretiakow D, Skorek A, Stodulski D. Trial proteomic qualitative and quantitative analysis of the protein matrix of submandibular sialoliths. Molecules. 2021;26(21).

36.   Busso CS, Guidry JJ, Gonzalez JJ, Zorba V, Son LS, Winsauer PJ, et al. A comprehensive analysis of sialolith proteins and the clinical implications. Clin Proteomics. 2020;17:12.

37.   Izumi M, Zhang BX, Dean DD, Lin AL, Saunders MJ, Hazuda HP, et al. Secretion of salivary statherin is compromised in uncontrolled diabetic patients. BBA Clin. 2015;3:135-40.

38.   Aqrawi LA, Galtung HK, Vestad B, Øvstebø R, Thiede B, Rusthen S, et al. Identification of potential saliva and tear biomarkers in primary Sjögren's syndrome, utilising the extraction of extracellular vesicles and proteomics analysis. Arthritis Res Ther. 2017;19(1):14.

39.   Inzitari R, Vento G, Capoluongo E, Boccacci S, Fanali C, Cabras T, et al. Proteomic analysis of salivary acidic proline-rich proteins in human preterm and at-term newborns. J Proteome Res. 2007;6(4):1371-7.

40.   Jin YJ, Han YE, Choi HG. The association between sialolithiasis and smoking, alcohol drinking and obesity in Korea: a nested case-control study. BMC Public Health. 2020;20(1):516.

41.   Larsen T, Fiehn NE. Dental biofilm infections - an update. APMIS. 2017;125(4):376-84.

42.   Cho BH, Jung YH, Hwang JJ. Maxillary antroliths detected by cone-beam computed tomography in an adult dental population. Imaging Sci Dent. 2019;49(1):59-63.

43.   Penescu M, Purcarea VL, Sisu I, Sisu E. Mass spectrometry and renal calculi. J Med Life. 2010;3(2):128-36.

44.   Xie B, Halter TJ, Borah BM, Nancollas GH. Aggregation of calcium phosphate and oxalate phases in the formation of renal stones. Cryst Growth Des. 2015;15(1):204-11.

45.   Takeda Y. Crystalloids with calcareous deposition in the parotid gland: one of the possible causes of development of salivary calculi. J Oral Pathol.

1986;15(8):459-61.

46.   Nolasco P, Anjos AJ, Marques JM, Cabrita F, da Costa EC, Maurício A, et al. Structure and growth of sialoliths: computed microtomography and electron microscopy investigation of 30 specimens. Microsc Microanal. 2013;19(5):1190-203.

47.   Kasaboğlu O, Er N, Tümer C, Akkocaoğlu M. Micromorphology of sialoliths in submandibular salivary gland: a scanning electron microscope and X-ray diffraction analysis. J Oral Maxillofac Surg. 2004;62(10):1253-8.

48.   Liesegang RE. Uber einige eigenschaften von gallerten. Naturwissensch Wochenschr. 1896;11:353-62.

49.   Ostwald W. Zur theorie der Liesegang'schen Ringe. Kolloid-Zeitschrift. 1925;36(1):380-90.

50.   Łępicka M, Rodziewicz M, Kawalec M, Nowicka K, Tsybrii Y, Kurzydłowski KJ. Diatomaceous earth as a drug-loaded carrier in a glass-ionomer cement. J Mech Behav Biomed Mater. 2022;133:105324.

51.   Zhang X, Yang H, Li S, Qin G, Yang L. Natural diatomite particles: size-, dose- and shape- dependent cytotoxicity and reinforcing effect on injectable bone cement. J Mater Sci Technol. 2018;34(6):1044-53.

52.   Brody G, Yale K, Slater LJ, Lanzon J, Carey DL, Ragsdale BD. A case of oral foreign-body granuloma due to diatoms. J Cutan Pathol. 2021;48(3):429-33.

53.   Jayasree RS, Gupta AK, Vivek V, Nayar VU. Spectroscopic and thermal analysis of a submandibular sialolith of Wharton's duct resected using Nd:YAG laser. Lasers Med Sci. 2008;23(2):125-31.

54.   Giray CB, Dogan M, Akalin A, Baltrusaitis J, Chan DCN, Skinner HCW, et al. Sialolith characterization by scanning electron microscopy and X-ray photoelectron spectroscopy. Scanning. 2007;29(5):206-10.

55.   Mimura M, Tanaka N, Ichinose S, Kimijima Y, Amagasa T. Possible etiology of calculi formation in salivary glands: biophysical analysis of calculus. Med Mol Morphol. 2005;38(3):189-95.

Tables

Table 1. Patient demographic information.

No	Sex	Age	PMH	Symptoms	Location	Anesthesia	Treatment	Biopsy Results
A1	F	22	Not specific	Came for impacted third molar removal	Hilar portion of right SMG	GA	Sialoendoscopy and surgical extraction of #18,38,48 teeth	~
A2	F	38	Hypothyroidism	~	Left Wharton's duct orifice		Sialolithotomy	
A3	F	34	Not specific	Came for impacted third molar removal	Hilar portion of left SMG	GA	Sialolithotomy and surgical extraction of #18,48 teeth	~
A4	F	21	Not specific	Pain and swelling in the right submandibular area	Hilar portion of right SMG	GA	Sialolithotomy and surgical extraction of #38,48	~
A5	F	24	Not specific	Discomfort in the left SMG area	Hilar portion of left SMG	GA	Sialolithotomy and ductoplasty	~
A6-1	F	48	Not specific	Swelling in the right SMG area	Hilar portion of right SMG	~	Spontaneously came out	~
A6-2	F	50	Not specific	~	Hilar portion of right SMG	~	Sialoendoscopy and ductoplasty on right SMG	
A7	F	20	Not specific	Swelling and pain in the right submandibular salivary gland area	Hilar portion of SMG (both sides); tonsils (both sides)	GA	Sialolithotomy, tonsillectomy	Tonsil, right, tonsillectomy; Tonsillar hyperplasia.
A8	M	55	Not specific	Swelling in the sublingual area	Left Wharton's duct orifice	IV	Sialolith removal	
A9	M	63	HCV, HTN	Pain and swelling in the	Left Wharton's duct	IV	Sialolithotomy	SMG mass excision;

40

				left submandibular salivary gland area	orifice			Sialolith.
A10	F	28	Not specific	Recurrent tender swelling for two years	Left Wharton's duct orifice	IV	Sialolithotomy (left SMG)	
A11	F	28	Not specific	Came for impacted third molar removal	Hilar portion of right SMG	IV	Sialolithotomy (right SMG)	
A12	F	29	Not specific	Swelling and pain in the sublingual area	Left Wharton's duct orifice	~	Sialolithotomy (left SMG)	
A13	F	7	Not specific	Pain and swelling due to yellowish hard mass on right Wharton's duct orifice	Right Wharton's duct orifice		Minor sialolithotomy	
A14	F	48	Not specific	Pain upon swallowing saliva or eating food, limited mouth opening.	Hilar portion of right SMG	IV	Sialolithotomy (right SMG)	SMG area, right, biopsy; Chronic sialodochitis.
A15	M	29	Not specific	Swelling	Hilar portion of right SMG	IV		
A16-1; 16-2	M	39	Not specific	Sore throat, pain upon swallowing	Both SMG hilum area	GA	Sialolithotomy, ductoplasty	
A17	M	47	Not specific	Pain and swelling	Hilar portion of left SMG	IV	Sialolithotomy	Recurrent sialolithiasis
A18	M	68	Hyperlipidemia, allergic rhinitis	Pain and swelling	Left Stensen's duct orifice	IV	Endoscopic assisted sialolithotomy, ductoplasty	

41

A19	M	21	Not specific	Pain and swelling	Hilar portion of left SMG	IV	Sialolithotomy	
A20	F	30		Discomfort	Hilar portion of right SMG	GA	Sialolithotomy and ductoplasty	
B1	M	53	HTN	Numbness in the left mandible area	Right tonsil; #36 extraction socket area	GA	Tonsillolith removal, Saucerization	1. Tonsillar tissue, right, tonsillolith removal; Chronic tonsillitis. 2. Mandible, left, saucerization; Chronic inflammation.
C1	M	48	Not specific	Nasal obstruction and pain	Right maxillary sinus	IV	MESS	Maxillary sinus, right, MESS; Chronic maxillary sinusitis
C2	M	60	Not specific	Nasal obstruction and pain	Left maxillary sinus	GA	MESS and mass excision	

GA, general anesthesia; IV, intravenous sedation; SMG, submandibular salivary gland; HTN, hypertension; MESS, modified endoscopy-assisted sinus surgery

Table 2. Morphometric parameters analyzed with micro-CT

Group	TV (mm^3)	Obj. V(mm^3)	Obj.V/TV %	TS (mm^2)	Obj.S (mm^2)	Obj.S/Obj.V (mm^{-1})	Obj.S/TV (mm^{-1})	St.Th (mm)	St.Sp (mm)	Po(tot) (%)
Group A	357.63±414.41	136.76±137.74	46.29±21.19	268.41±221.85	834.69±1200.21	3.07±4.07	0.83±0.93	0.81±0.36	0.96±0.62	54.15±21.14
Group B	60.60±0.00	50.00±00	82.51±0.00	109.98±0.00	260.60±0.00	0.01±0.00	0.00±0.00	0.52±0.00	0.19±0.00	17.49±0.00
Group C	319.84±387.55	102.53±129.19	50.05±21.96	257.07±208.96	773.67±1100.15	2.56±4.53	0.69±0.90	0.76±0.36	0.86±0.61	50.33±21.99
P value	0.663	0.816	0.208	0.782	0.863	0.578	0.370	0.458	0.282	0.197

TV, total VOI (volume of interest) volume; Obj. V, object volume; Obj.V/TV, percent object volume; TS, total VOI surface; Obj.S, object surface; Obj/S/Obj.V, object surface/ volume ratio; Obj.S/TV, object surface density; St.Th, structure thickness; St.Sp, structure separation; Po(tot), total porosity (percent)
One-way ANOVA test was used for comparison between groups

Table 3. Comparison level of Ca, C, O and P between the groups

	Weight percentage (wt%)				Atomic percentage (at%)			
	Ca	C	P	O	Ca	C	P	O
Group A	20.72±5.53	21.36±4.50	11.08±6.57	36.77±7.63	9.55±2.77	31.85±5.29	6.97±4.18	42.03±9.27
Group B	17.48±3.02	15.33±4.50	13.75±4.86	38.31±2.70	8.23±1.51	23.92±6.40	8.45±3.14	45.95±3.46
Group C	17.18±6.98	32.86±17.60	4.79±4.53	29.24±3.21	7.28±3.31	43.23±17.25	2.63±2.47	30.52±4.33
p value	0.258	0.006*	0.233	0.016*	0.153	0.004*	0.217	0.002*

One-way ANOVA test was used for comparison between groups

* $p < 0.05$ were considered statistically significant

Table 4. Elemental composition of the specimen in Group A, B and C

	Weight percentage				Atom percentage			
	Group A	Group B	Group C	p value	Group A	Group B	Group C	p value
Ca	20.72±5.31	17.48±3.02	17.18±6.98	0.258	9.55±2.77	8.22±1.51	7.28±3.31	0.153
C	22.36±4.50	15.33±.02	31.98±16.64	0.006*	31.85±5.29	23.92±6.40	40.00±19.24	0.039*
O	36.77±7.63	38.31±0.70	29.24±3.21	0.016*	42.03±9.27	45.95±3.46	30.52±4.33	0.002*
Cu	13.39±0.00	~	~	~	4.62±0.00	~	~	~
F	5.89±1.30	2.15±0.00	10.38±4.24	0.137	6.08±.1.27	2.2±0.00	9.59±4.17	0.194
N	14.68±5.63	7.93±3.39	7.93±3.39	0.031*	17.77±6.33	10.47±3.90	14.78±5.39	0.114
Na	2.22±0.47	2.27±0.72	3.81±2.49	0.178	1.89±4.18	1.85±0.53	2.89±2.02	0.311
P	11.08±6.57	13.75±4.86	4.79±4.53	0.233	6.97±4.18	8.45±3.14	2.63±2.48	0.217
Si	9.29±6.59	5.74±4.43	3.76±2.88	0.158	6.16±4.50	3.61±2.69	2.34±1.86	0.139
Zn	10.68±0.00	~	~	~	3.59±0.00	~	~	~
Zr	7.41±0.00	3.51±0.00	~	~	1.59±0.00	0.75±0.00		
Fe	~	0.87±0.00	~	~	~	0.30±0.00	~	~
Mg	1.76±0.28	2.54±0.53	2.89±1.54	0.182	1.41±0.23	1.96±0.36	2.09±1.15	0.283

One-way ANOVA test was used for comparison between groups
*$p < 0.05$ were considered statistically significant

Table 5. Elemental composition of the sialolith specimen of group A at the peripheral, middle and core regions

	Weight percentage (wt%)				Atom percentage (at%)			
	Periphery	Middle	Core	p value	Periphery	Middle	Core	p value
Ca	19.97±4.36	20.73±4.37	22.15±8.50	0.826	9.58±2.04	9.25±2.53	10.28±4.06	0.817
C	21.19±2.53	40.08±4.79	36.53±4.39	0.585	34.00±5.18	32.09±5.36	30.36±5.59	0.531
O	33.24±13.26	40.08±4.79	36.54±4.39	0.19	39.54±15.93	39.54±15.63	41.61±5.87	0.952
Cu	13.39±0.00	~	~		4.62±0.00	~	~	~
F	6.64±0.11	4.39±0.00	~	0.037*	6.81±0.13	4.62±0.00	~	0.048*
N	12.22±8.54	15.71±3.03	15.41±7.41	0.720	15.62±8.60	18.29±3.21	19.06±9.47	0.808
Na	2.22±0.55	2.61±0.00	2.56±0.09	0.531	2.23±0.00	2.23±0.00	2.18±0.09	0.833
P	12.58±6.88	8.10±10.77	12.03±6.31	0.804	11.07±0.00	5.22±6.99	7.42±3.94	0.650
Si	9.12±7.54	10.02±6.66	9.66±6.00	0.978	6.77±6.05	6.49±4.26	5.96±2.99	0.974
Zn	10.68±0.00	~	~	~	3.59±0.00	~	~	~
Zr	7.41±0.00	~	~	~	1.59±0.00	~	~	~
Mg	1.76±0.00	1.76±0.00	10.72±7.38	0.531	1.42±0.00	0.99±0.00	6.78±4.34	0.502

One-way ANOVA test was used for comparison between groups
p <0.05 were considered statistically significant

Table 6. Elemental composition of the tonsillolith specimen of group B at the peripheral, middle and core regions

	Weight percentage (wt%)				Atom percentage (at%)			
	Periphery	Middle	Core	p value	Periphery	Middle	Core	p value
Ca	17.15±0.00	17.07±0.00	17.72±4.25	0.988	8.17±0.00	8.19±0.00	8.26±2.13	0.999
C	13.93±0.00	41.88±0.00	17.32±0.00	0.572	22.14±0.00	17.23±0.00	26.74±0.00	0.562
O	31.01±0.00	41.88±0.00	37.56±2.55	0.446	44.17±0.00	50.36±0.00	45.08±3.39	0.481
F	~	~	2.15±0.00	~	~	~	2.20±0.00	~
N	6.87±0.00	5.95±0.00	11.75±6.17	0.687	9.37±0.00	8.17±0.00	14.53±6.84	0.698
Na	2.01±0.00	1.71±0.00	2.44±4.03	0.802	1.67±0.00	1.43±0.00	1.96±0.72	0.814
P	18.03±0.00	18.08±0.00	10.88±4.03	0.345	11.12±0.00	11.23±0.00	6.64±2.70	0.372
Si	1.63±0.00	2.21±0.00	4.82±0.00	0.316	1.11±0.00	1.51±0.00	3.19±1.01	0.321
Zr	~	~	3.51±0.00	~	~	~	0.75±0.00	~
Fe	0.87±0.00	~	~	~	0.30±0.00	~	~	~
Mg	2.48±0.00	2.36±0.00	2.62±0.72	0.950	1.95±0.00	1.86±0.00	1.10±0.51	0.973

One-way ANOVA test was used for comparison between groups
$p < 0.05$ were considered statistically significant

Table 7. Elemental composition of the antrolith specimen of group C at the peripheral, middle and core regions

	Weight percentage (wt%)				Atomic percentage (at%)			
	Periphery	Middle	Core	p value	Periphery	Middle	Core	p value
Ca	13.10±0.33	14.91±13.20	20.35±5.26	0.494	5.18±0.66	6.44±6.48	8.75±2.25	0.492
C	36.04±18.83	45.45±33.94	24.98±5.07	0.455	46.22±19.90	54.95±31.69	35.87±7.61	0.496
O	32.48±4.69	30.29±1.57	26.48±1.40	0.045*	32.37±7.93	31.26±6.39	28.24±1.36	0.492
F	4.86±0.00	15.18±0.00	10.74±0.33	0.044*	4.35±0.00	14.55±0.00	9.72±0.27	0.037*
N	8.15±1.96	~	15.20±1.87	0.027*	9.33±.17	~	18.41±1.86	0.025*
Na	2.04±0.55	4.08±5.17	4.93±0.58	0.535	1.42±0.52	1.42±0.52	3.75±0.54	0.012*
P	7.99±0.00	~	1.58±0.00	~	4.38±0.00	~	0.88±0.00	~
Si	4.09±5.51	~	5.39±2.31	0.726	2.24±3.03	~	3.38±1.54	0.604
Mg	0.93±0.00	~	3.55±0.99	0.150	0.65±0.00	~	2.56±0.79	0.170

One-way ANOVA test was used for comparison between groups
$p < 0.05$ were considered statistically significant

Figures and figure legends

Figure 1. Schematic drawing of the sialolith formation. Sialomicroliths are microscopic concretions of the salivary gland and are found in asymptomatic individuals. (A). During salivary stagnation or secretory inactivity, sialomicroliths at a certain size may cause ductal obstruction (B) leading to further inflammation, retrograde infection of bacteria, swelling, sclerosis and atrophy (C). At this time neutrophils enter the salivary gland and externalize their NETs, which attract and trap calcium-based crystals such hydroxyapatite, brushite, and whitlockite and promote the pathogenesis of sialolithiasis (D).
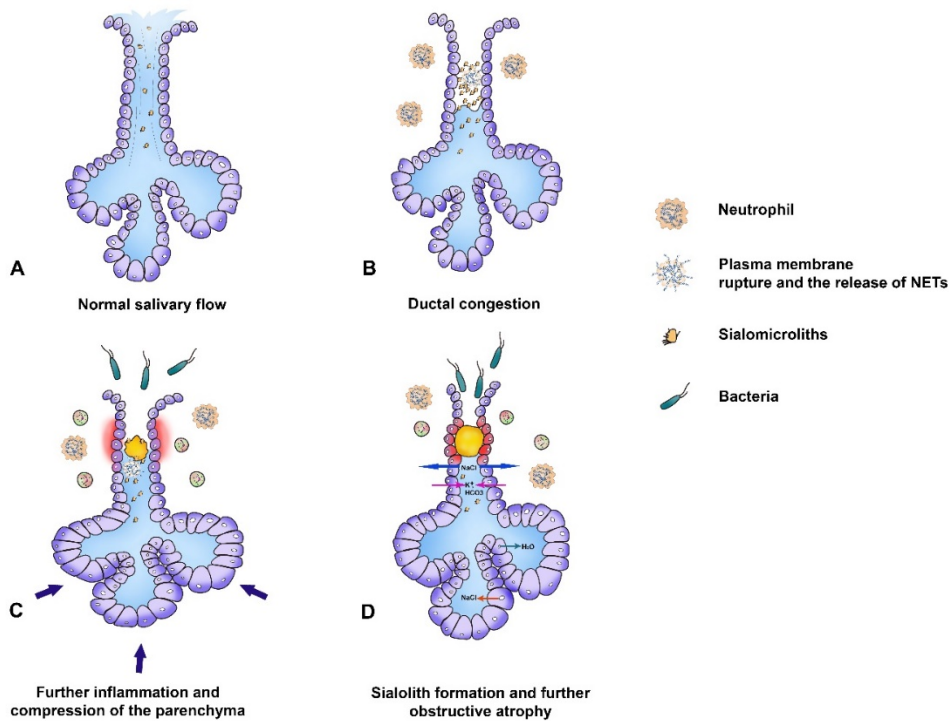
Figure 2. Schematic drawing of the tonsillolith formation. Adult palatine tonsils have an average of 10-20 crypts (A). These crypts become an anaerobic environment for bacterial accumulation (B). Tonsilloliths are similar in architecture and physiological behavior to dental biofilms (C). As the biofilm matures, the crypt dilates with inflammation (D).

A
Normal tonsillar crypt

B
Tonsil crypt become an anaerobic
environment for bacteria to accumulate and
form biofilms

Bacteria

Biofilm
formation

C
Bacteria adhere to a surface in moist
environment and are held together by an
extracellular polymeric substance

D
As the biofilm matures it dilates the
crypt to accommodate the tonsillolith
and cause inflammation

Figure 3. Schematic drawing of antrolith formation. Patent osteo-meatal unit (OMU) with drainage and ventilation of the maxillary sinus (A). The formation of antrolith may begin with the calcification of a nidus of endogenous origin, which continues to increase due to the precipitation of calcium salts in a sinus with obstructed OMU. (B). Precipitation of minerals around the nidus (C).

A — Patent osteo-meatal unit (OMU)

B — Obstructed OMU

C — Antrolith formation
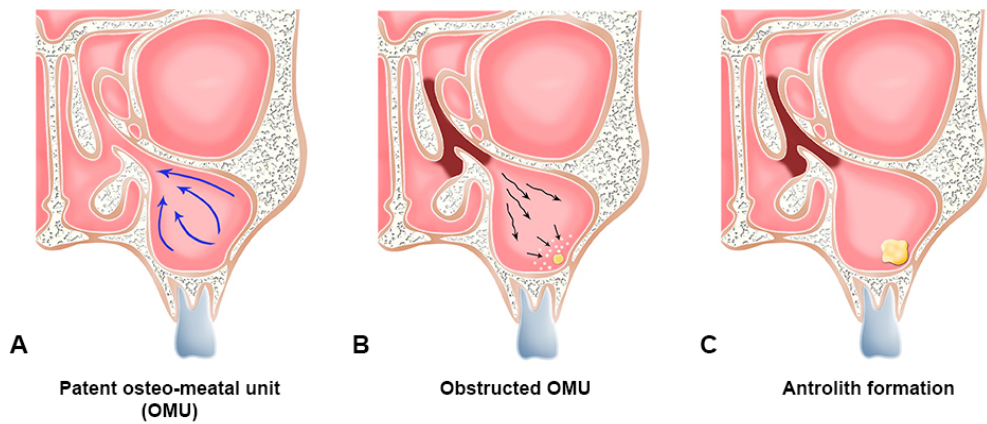
Figure 4. Clinical, two dimensional (2D) micro-CT cross section, and 3D reconstructed images of sialoliths A4, A5, A7, A8, A9, A10, A11, and A12. Sialoliths show onion-like concentric lamellar structure. Brighter regions represent higher mineralization and dark regions represent organic substance. Scale: 2 mm.
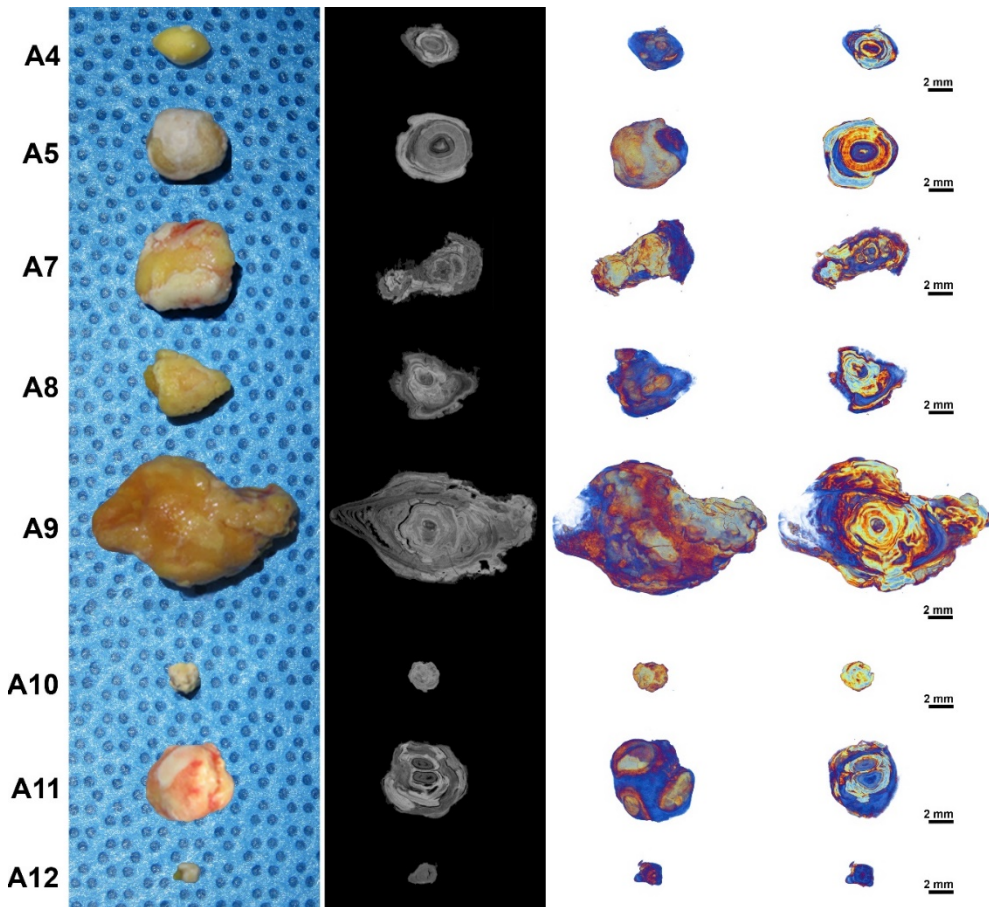
Figure 5. Clinical, 2D micro-CT cross section, and 3D reconstructed images of sialoliths A15, A16-1, A16-2, A18, A19, and A20. Scale: 2 mm.
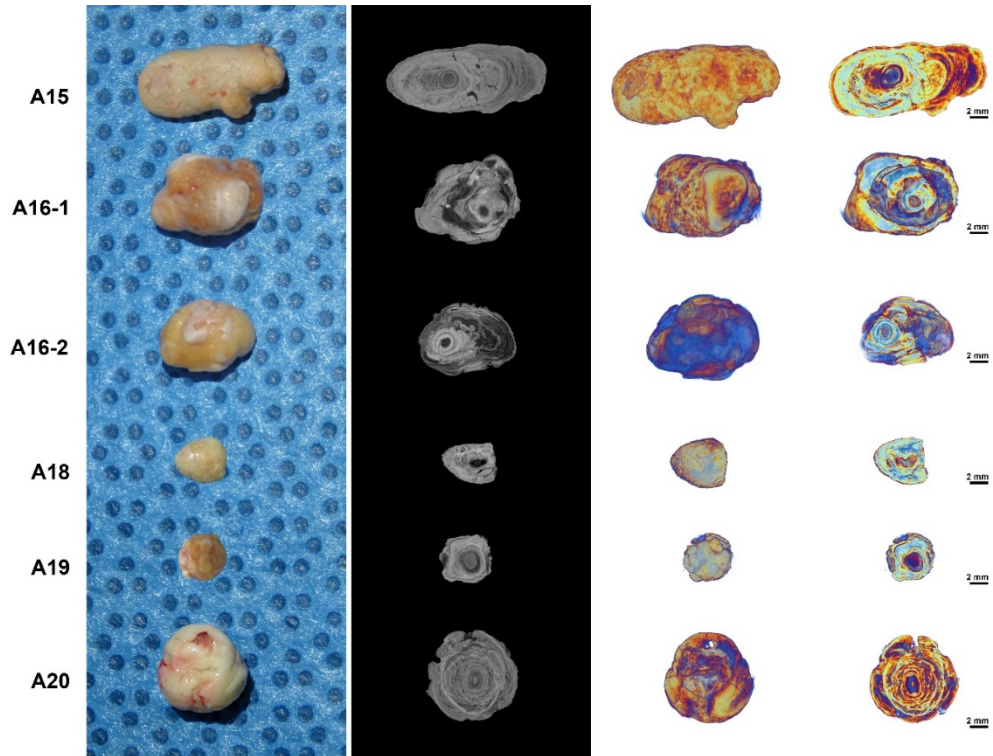
**Figure 6.** Clinical, 2D micro-CT cross section, and 3D reconstructed images of B1, C1, and C2 specimens. Scale: 2 mm.
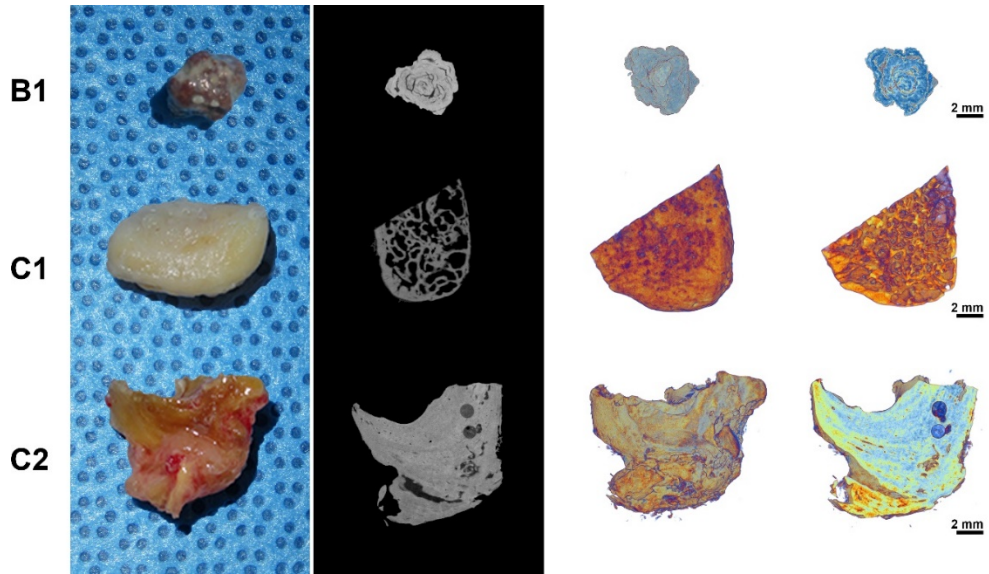
Figure 7. Representative histological findings of sialolith A1 with a highly mineralized single core, (H&E staining, 4×). Scale bar = 500 μm. (A). Eosinophilic core (black asterisk), (H&E staining, 20×). Scale bar = 50 μm (B). Mineralized nodules in the outer core (black arrowhead), (H&E staining, 20×). Scale bar = 50 μm (C). Tear-drop shaped globules (black arrows), (H&E staining, 20×). Scale bar = 50 μm (D). Less mineralized layers of sialolith stained with purple (red arrowhead), nodules undergoing mineralization (blue arrowhead), (H&E staining, 20×). Scale bar = 50 μm (E). Mineralized nodules (black arrowhead), (H&E staining, 20×). Scale bar = 50 μm (F).
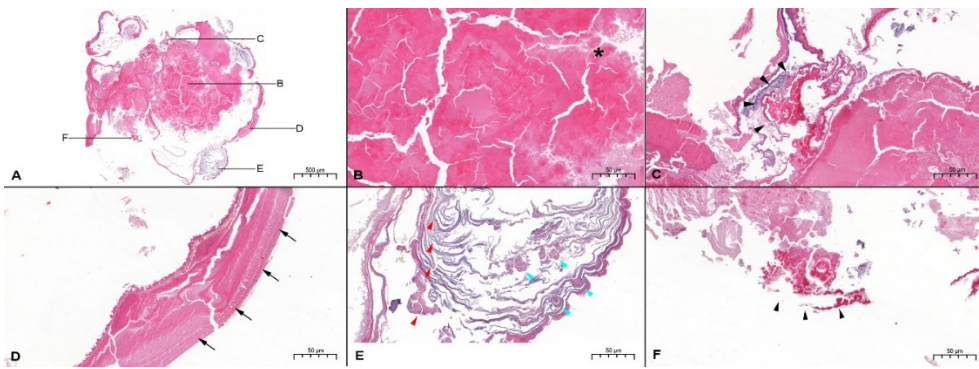
Figure 8. Representative histological findings of sialolith A2 with a single organic core where the core has been lost during the histological slide preparation, (H&E staining, 4×). Scale bar = 500 μm. (A). Globular lipid particles found near the core of the sialolith (black arrowhead), (H&E staining, 20×). Scale bar = 50 μm (B). Mineralized nodules were found in the outer layers of the core showing irregular mineralization (black arrow), (H&E staining, 20×). Scale bar = 50 μm (C). Amorphous basophilic materials at the outer layer, (H&E staining, 20×). Scale bar = 50 μm (D). Alternating irregular pattern of highly mineralized and less mineralized layers at the periphery of the sialolith (E), (H&E staining, 20×). Scale bar = 50 μm (E). Needle-like crystallization (yellow arrow), (H&E staining, 20×). Scale bar = 50 μm (F).
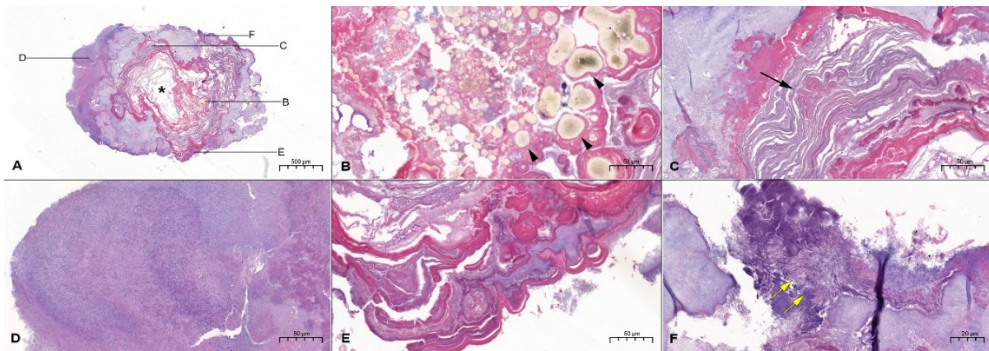
Figure 9. Representative histological findings of sialolith A3 with two cores (black arrow), (H&E staining, 4×). Scale bar = 500 μm. (A). The core found at the periphery of the sialolith showed a highly mineralized homogenous core (black asterisk), (H&E staining, 20×). Scale bar = 50 μm (B). The core found in the middle layer of the sialolith showed a highly mineralized core compared to the outer layers (black asterisk), (H&E staining, 20×). Scale bar = 50 μm (C). Globular structures (black arrowhead), (H&E staining, 20×). Scale bar = 50 μm (D). The branch at the outer layer consists of mineralized nodules (E), (H&E staining, 20×). Scale bar = 50 μm (E). Globular structures (yellow arrowhead), (H&E staining, 20×). Scale bar = 50 μm (F).
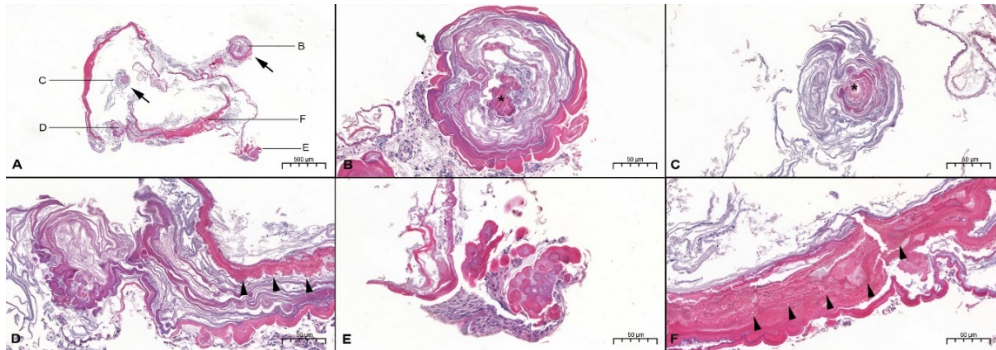
Figure 10. Representative histological findings of sialolith A6-1 showing no distinct core, (H&E staining, 4×). Scale bar = 500 μm. (A). Highly mineralized globular structures found in the center of sialolith (black arrow), (H&E staining, 20×). Scale bar = 50 μm (B). Details of amorphous basophilic materials found in the outer layer of the sialolith, (H&E staining, 20×). Scale bar = 50 μm (C). Detail of alternating layers of mineralized globular structures (black arrow), (H&E staining, 20×). Scale bar = 50 μm (D). Amorphous basophilic materials with mineralized nodule (black arrowhead) (E), (H&E staining, 20×). Scale bar = 50 μm (E). Globular structures in the middle layer (black arrowhead), (H&E staining, 20×). Scale bar = 50 μm (F).
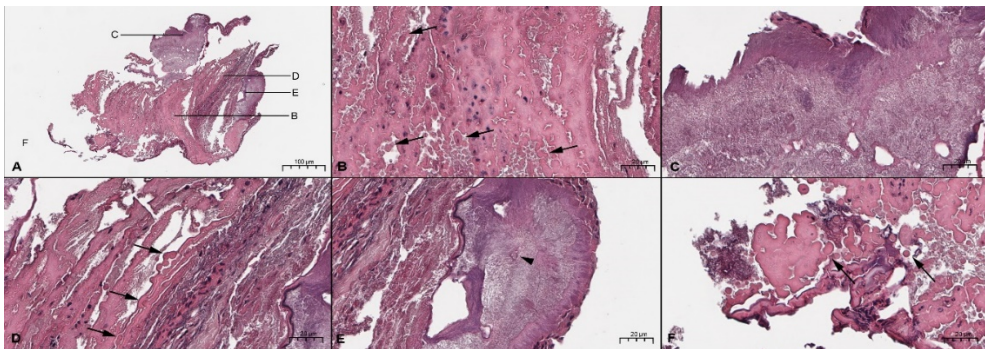
Figure 11. Representative histological findings of sialolith A6-2 showing no distinct core, (H&E staining, 4×). Scale bar = 500 μm. (A). A nodule with highly mineralized outer later (black asterisk), (H&E staining, 20×). Scale bar = 50 μm (B). Alternating layers of mineralized and less mineralized globular structures (H&E staining, 20×). Scale bar = 50 μm (C). Amorphous basophilic material at the periphery of the sialolith, (H&E staining, 20×). Scale bar = 50 μm (D). Globular structures in the outer layer (black arrowhead), (H&E staining, 20×). Scale bar = 50 μm (E-F).
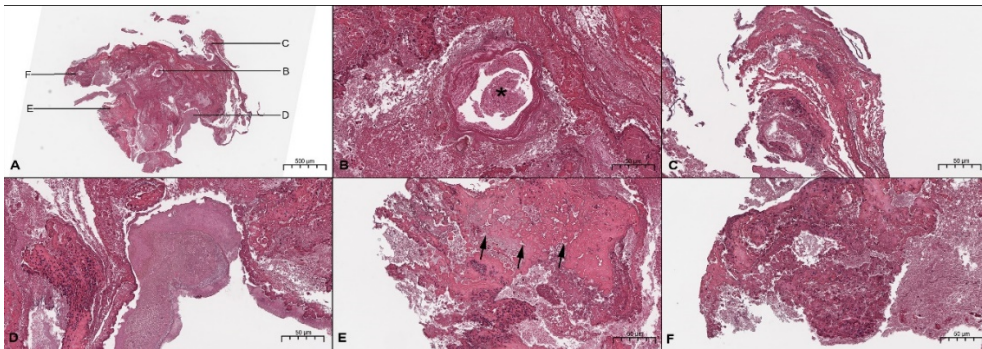
Figure 12. Representative histological findings of pediatric sialolith A13 with a highly mineralized single core, (H&E staining, 4×). Scale bar = 500 μm. (A). Eosinophilic core (H&E staining, 20×). Scale bar = 50 μm (B). Laminated structures with concentric pattern and mineralized nodules were observed in the periphery of the sialolith (H&E staining, 20×). Scale bar = 50 μm (C). Amorphous basophilic materials were observed at the middle layer of the sialolith (H&E staining, 20×). Scale bar = 50 μm (D). Mineralized nodules (black arrowhead), (H&E staining, 20×). Scale bar = 50 μm (E). Globular structures (black arrow), (H&E staining, 20×). Scale bar = 50 μm (F).
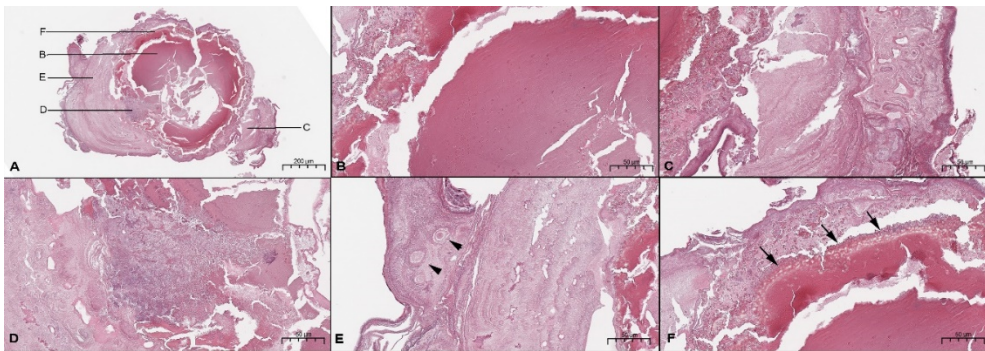
Figure 13. Representative histological findings of sialolith A14 with a single organic core where the core has been lost during the histological slide preparation (black asterisk), (H&E staining, 4×). Scale bar = 500 μm. (A). Thin layers of less mineralized structures, (H&E staining, 20×). Scale bar = 50 μm (B Amorphous basophilic material at the periphery of the sialolith, (H&E staining, 20×). Scale bar = 50 μm (C). Needle-like crystallization (black arrow), (H&E staining, 20×). Scale bar = 50 μm (D). Highly mineralized nodules (black arrowhead), (E), (H&E staining, 20×). Scale bar = 50 μm (E). Globular structures (black arrow), (H&E staining, 20×). Scale bar = 50 μm (F).
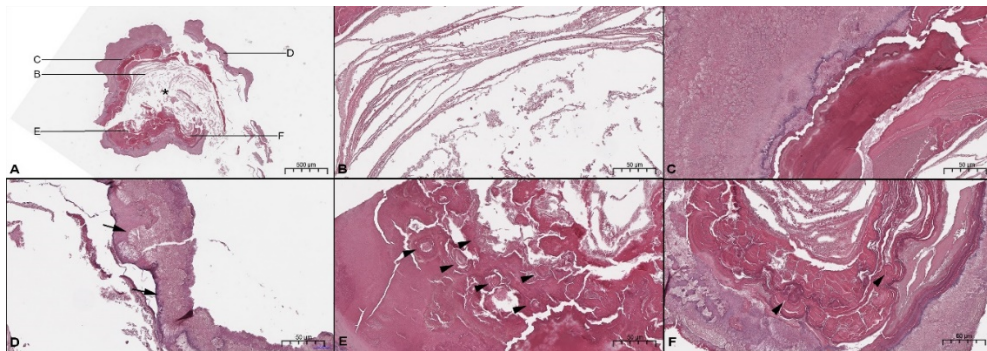
Figure 14. Histopathological findings of H&E stained tonsillolith specimen (B1), 2× (A). The overall specimen exhibits a crystalline structure of organic material at a mature stage of its development, 5× (B). A duct-like structure was observed at the center of squamous epithelium indicating the minor salivary gland duct, 20× (C). Squamous epithelium on the surface of the tonsillolith was noted to extend toward the lining of the tonsil crypt (yellow arrowheads), magnification 10×, 20×, 40×, respectively (D-F). At high magnifications the tonsillolith was composed of dense matrix, and microbial colonies were found composed of rods and cocci (red arrowheads), 10×, 20×, 40×, respectively (G-I).
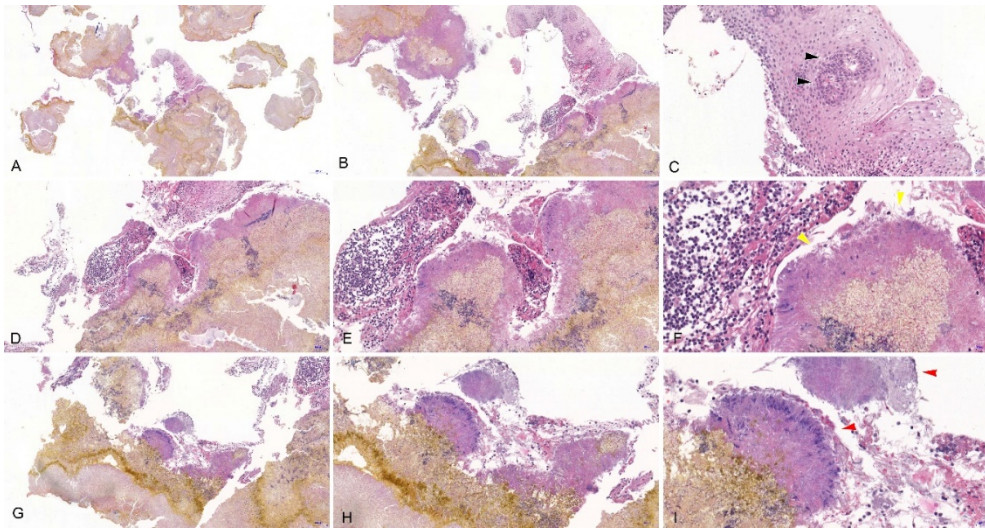
Figure 15. Histopathological findings of H&E stained antrolith (C1), 2x (A). The lesion was not encapsulated and showed a homogeneous lamellar bone with fibrous marrow cavities. The woven bone was replaced by lamellar bone with Haversian canals at the periphery, 10×, 20×, 40×, respectively (B-D). Inflamed granulation tissue with bone sequestrum, 2×, 10×, 20×, 40×, respectively (E-H).
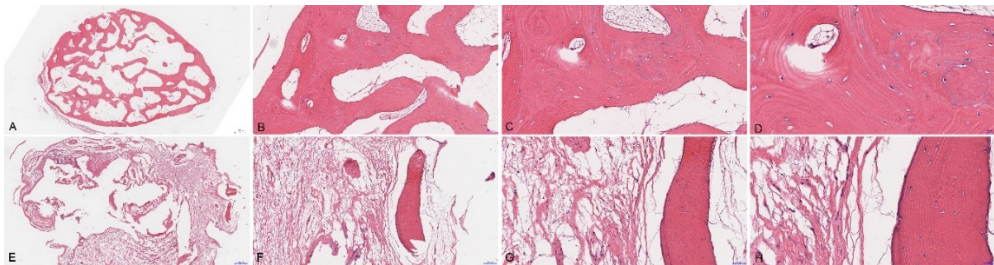
Figure 16. Scanning electron microscopy (SEM) images of seven exemplary stones at 50× magnification. Submandibular gland sialolith A5 (A). Sialolith from the right submandibular salivary gland in A11 (B). Salivary gland stone from the right submandibular salivary gland in A12 (C). Recurrent salivary stone from the left submandibular salivary gland in A15 (D). Tonsillolith (E). Antrolith from the right maxillary sinus in C1(F). Antrolith C2 (G).
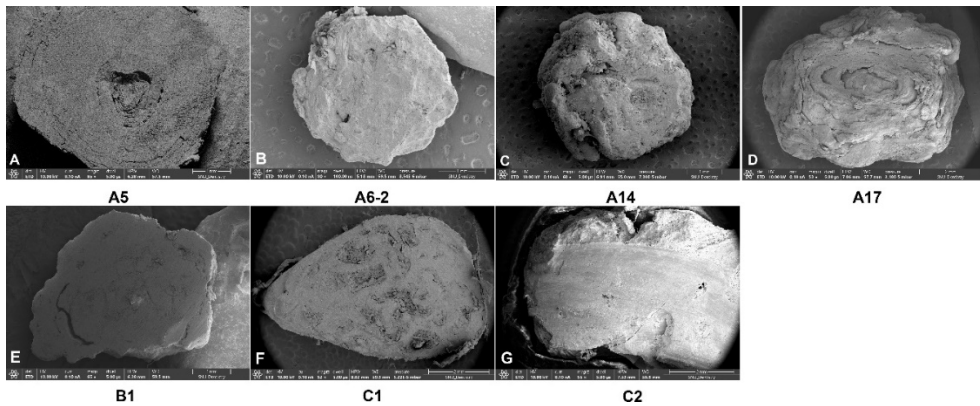
Figure 17. Combined SEM images at 500× magnification of sialolith (A5) with 05 focused points of interest. Irregular structure seen at the periphery of the sialolith at point 01. A plate-like structure was observed on the point 02. Globular structure seen at the core of the sialolith (yellow arrowhead).
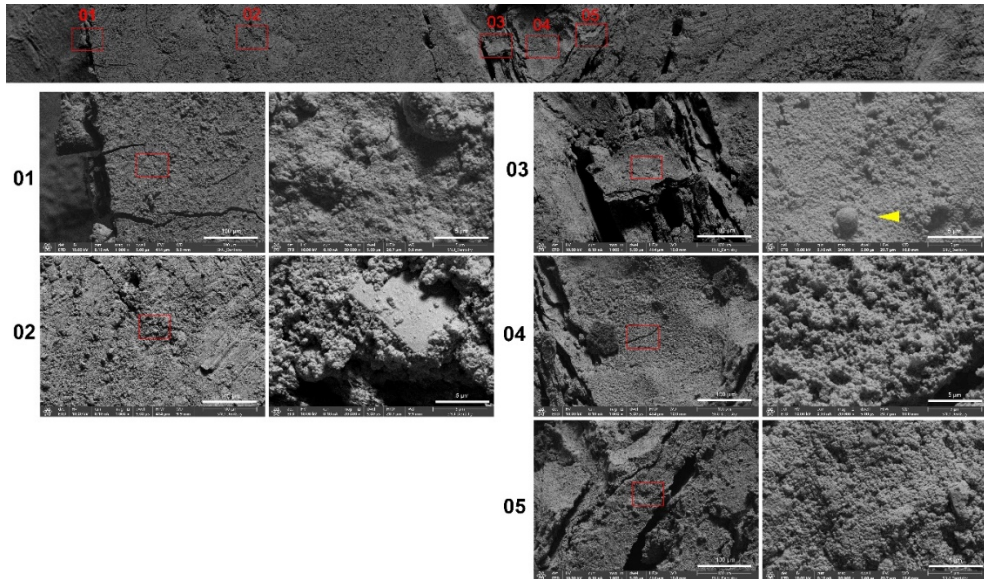
Figure 18. Combined SEM images at 500× magnification of sialolith A6-2 with 14 points of interest.
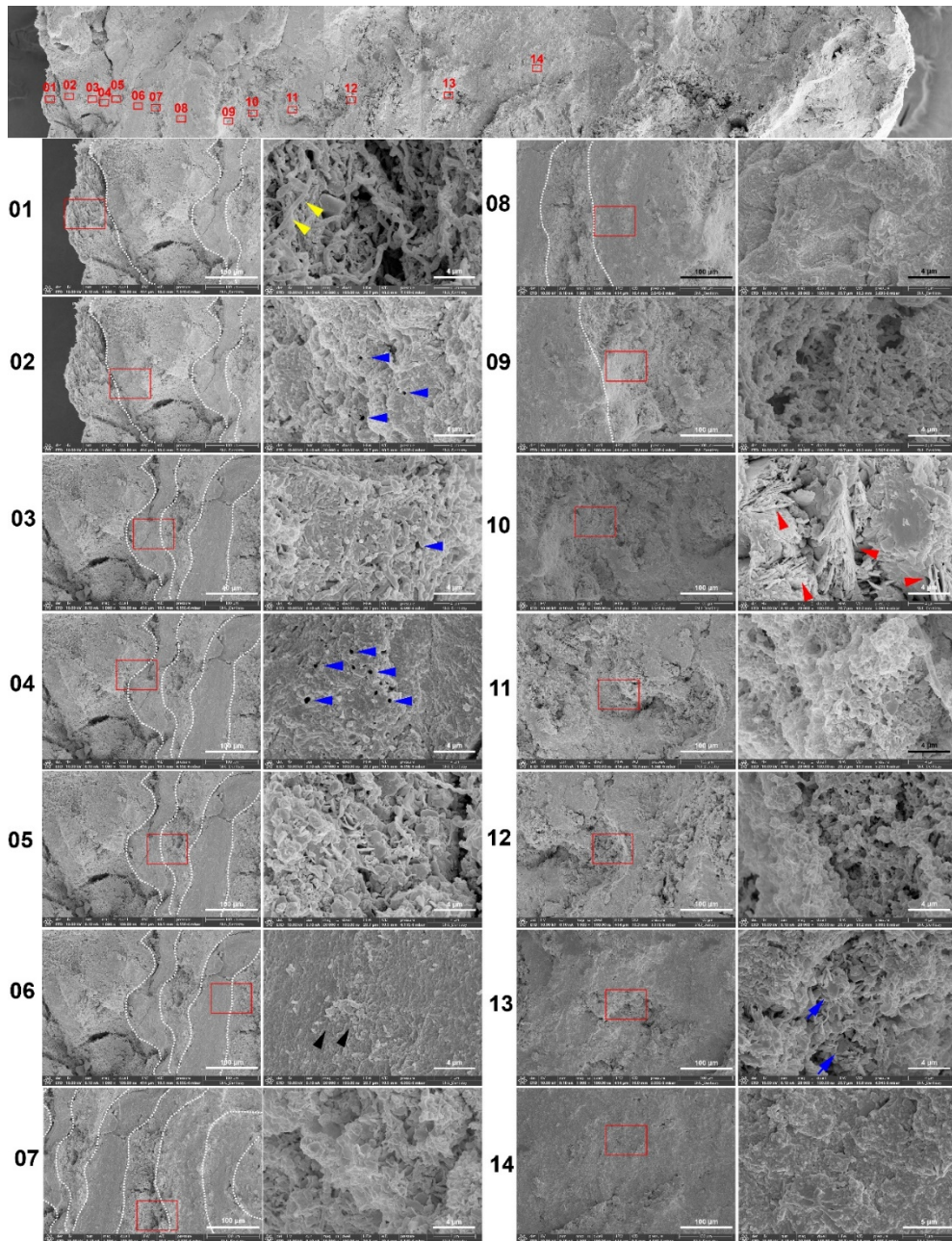
Figure 19. Combined SEM images at 500× magnification of sialolith A14 with 08 focused points of interest. Alternating layers of organic and inorganic/mineralized bands are observed. Suggested colony of elongated bacteria at the surface of the stone from point 01 at 20,000× magnification. Irregularly shaped structure formation from point 03 at 20,000× magnification. Denser highly mineralized structure is seen on points 03, 04. Bacterial biofilm with single calcite-like crystal from point 05 at 20,000× magnification (blue arrowhead). Irregularly shaped structure formation from point 08 at 20,000× magnification.
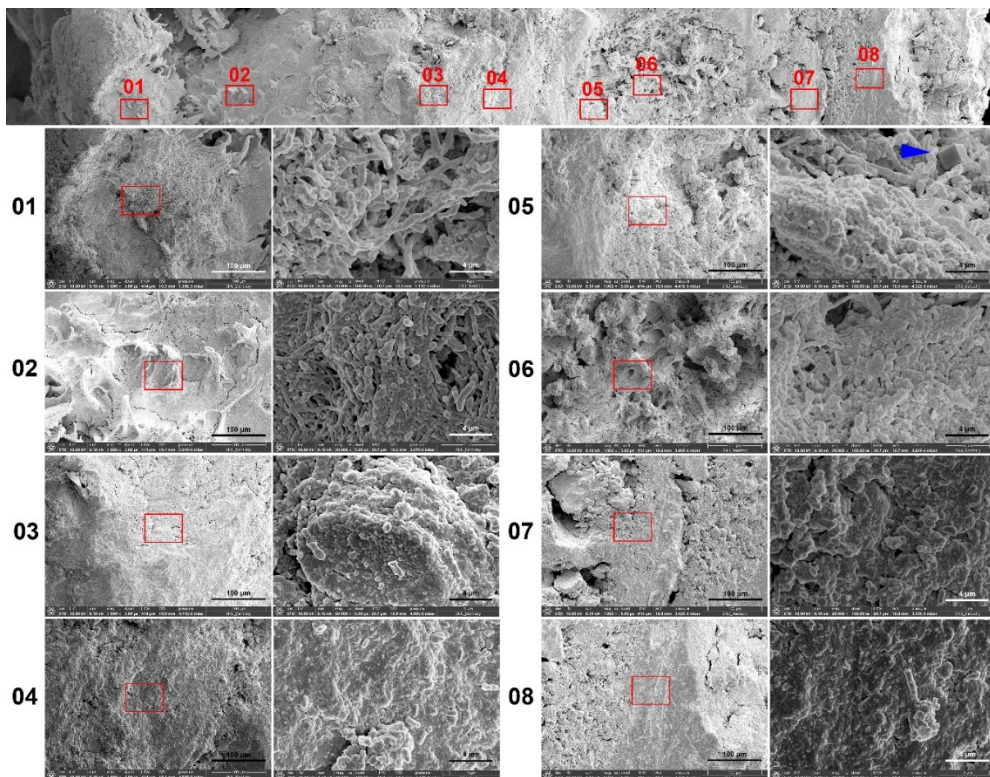
Figure 20. Combined SEM images at 500× magnification of sialolith A17 with 13 points of interest.
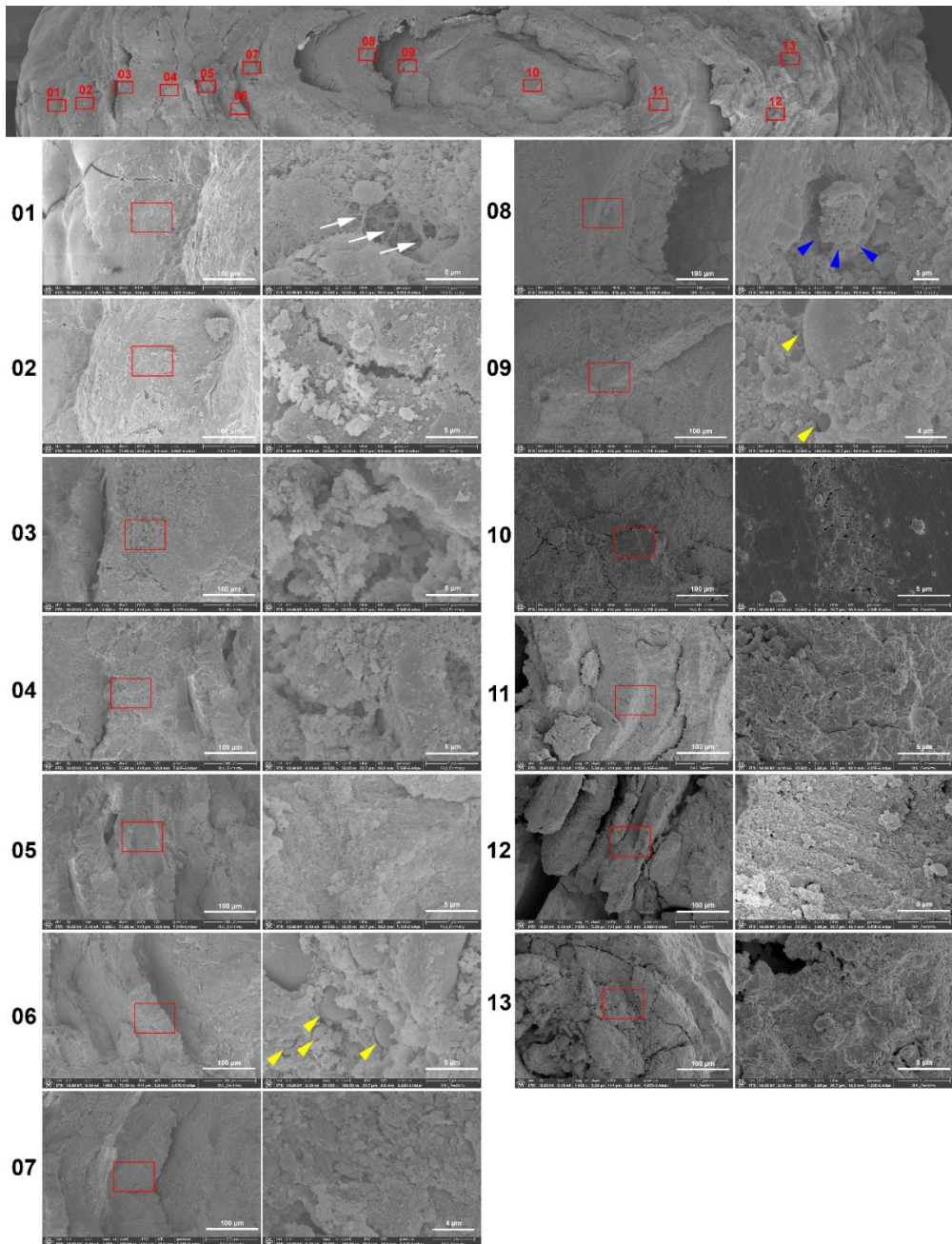
Figure 21. Backs scattered electron images of A17.
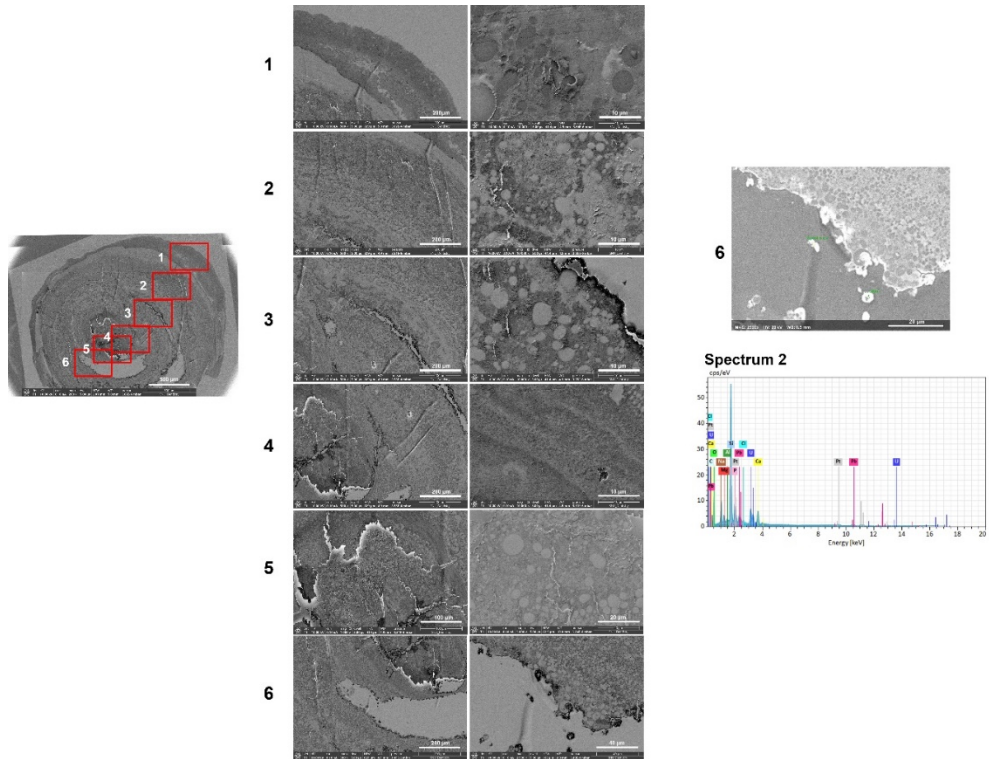
Figure 22. Combined SEM images at 500× magnification of tonsillolith (B1) from group B cross-sectional surface at the center with the marking of ten focal points of interest.
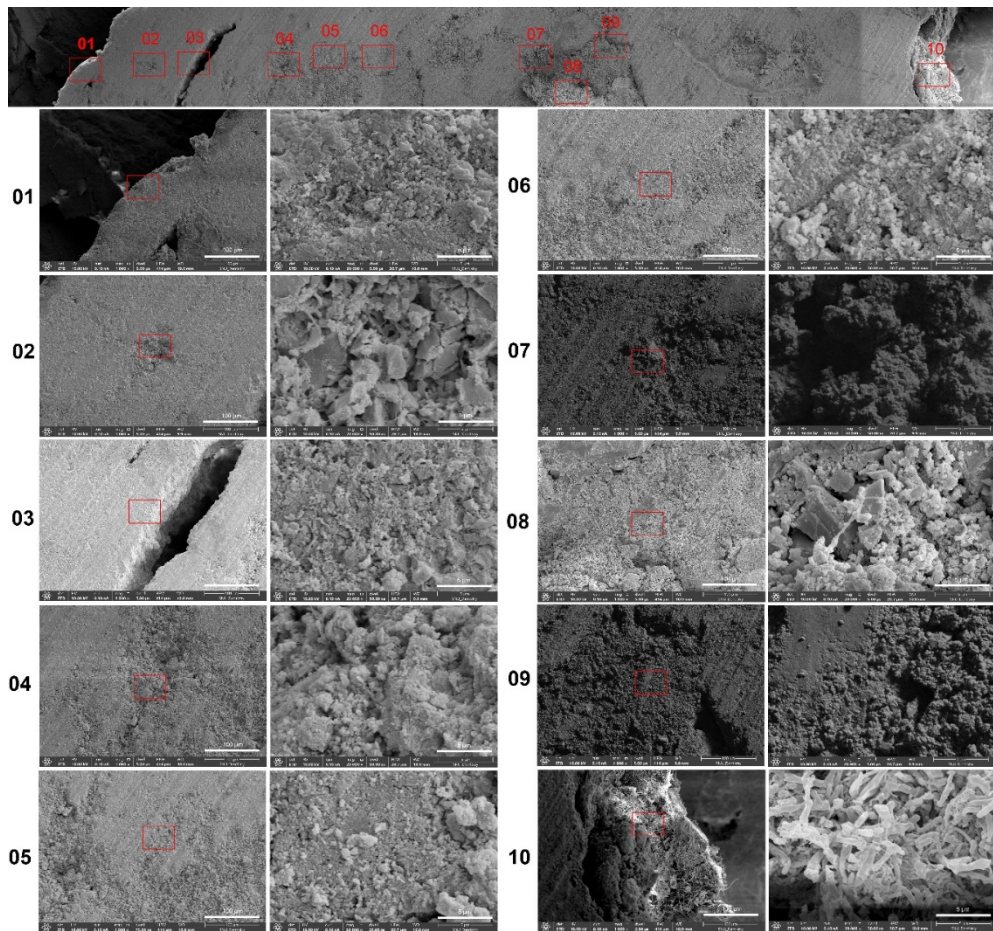
Fi**gure 23.** Combined SEM images at 500× magnification of antrolith (C1) from group C cross-sectional surface at the center with the marking of 14 focal points of interest.
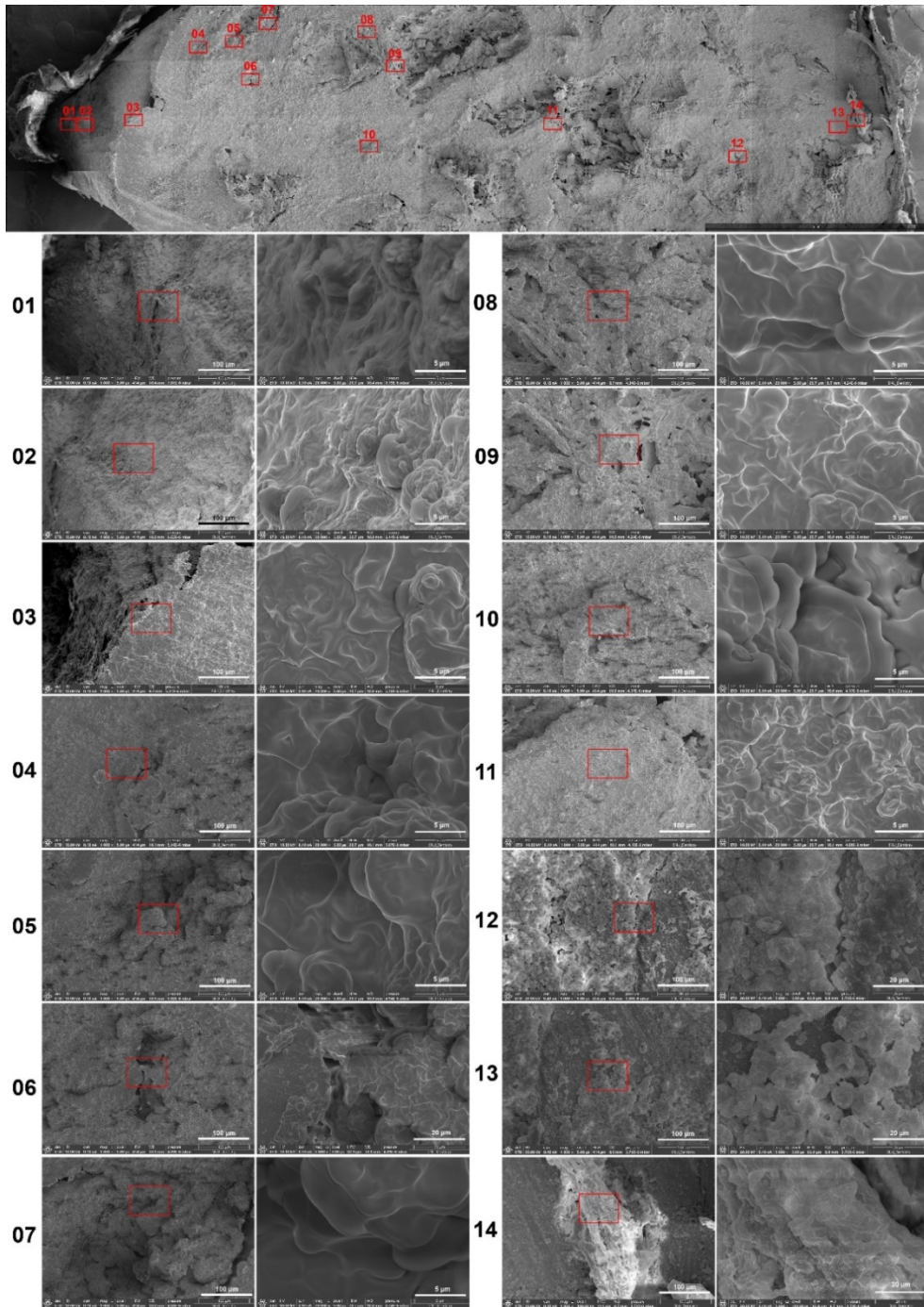
Figure **24.** Combined SEM images at 500× magnification of antrolith (C2) from group C cross-sectional surface at the center with the marking seven focal points of interest.
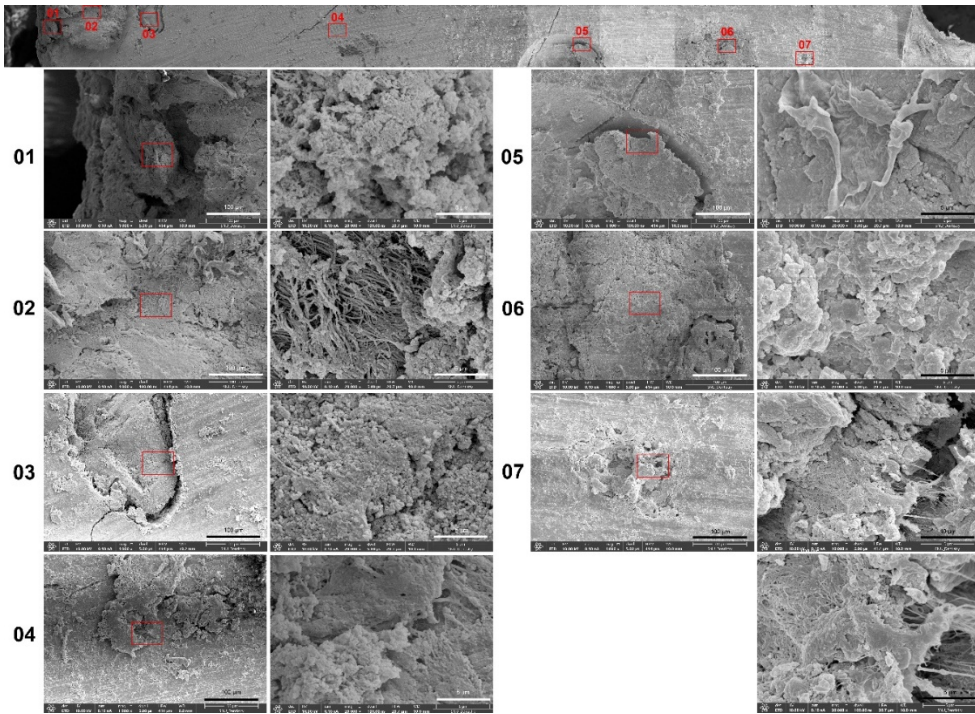
Figure 25. Mapping of elemental distribution and a spectrum of the representative points with EDS results in sialolith A5. SEM image, 10,000× magnification. EDS analyses were carried out on five representative points of interest on the peripheral (P), middle (M), and core (C) layers. The major elements observed in the specimen were Ca, P, O, and C. A non-homogeneous distribution of Si and Ca were found at 02-M point of interest.
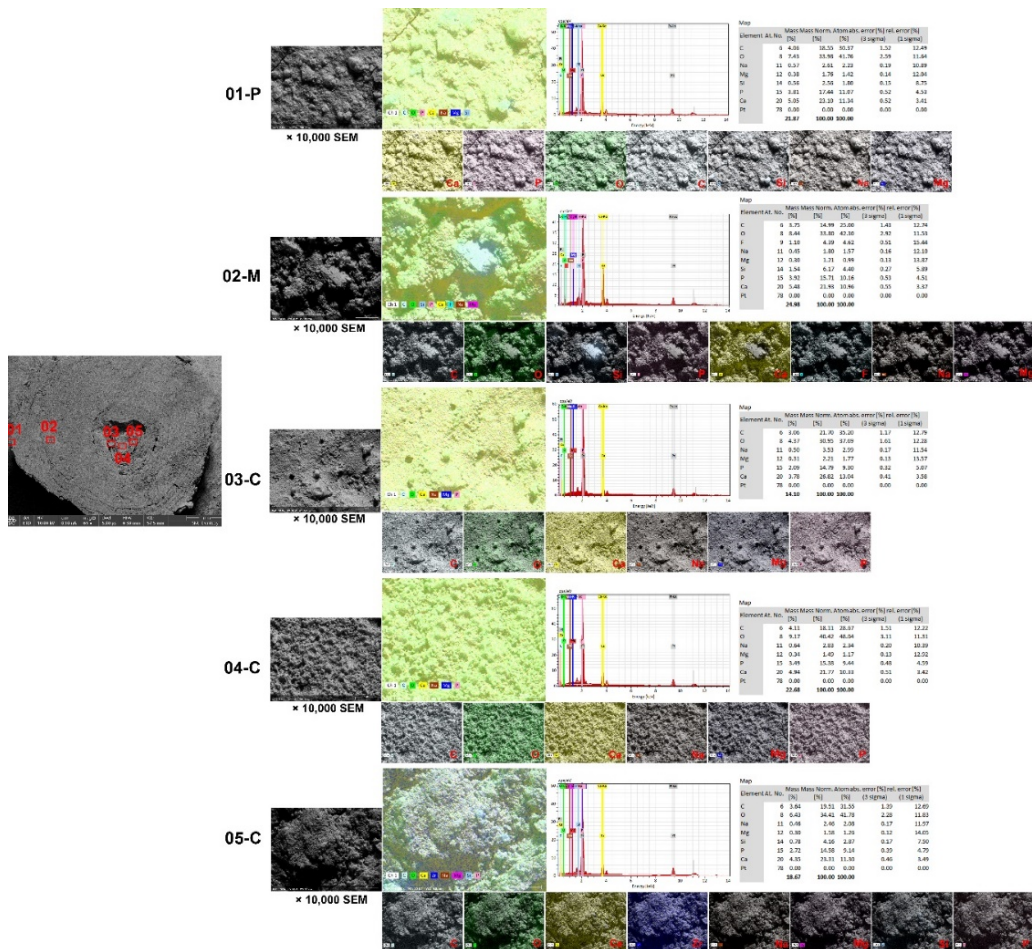
Figure 26. Mapping of elemental distribution and a spectrum of the representative points with EDS results in sialolith A6-1. SEM image, 10,000× magnification. EDS analyses were carried out on five representative points of interest on the peripheral (P), middle (M), and core (C) layers. A non-homogeneous distribution of O and Ca was found at 01-P point of interest.
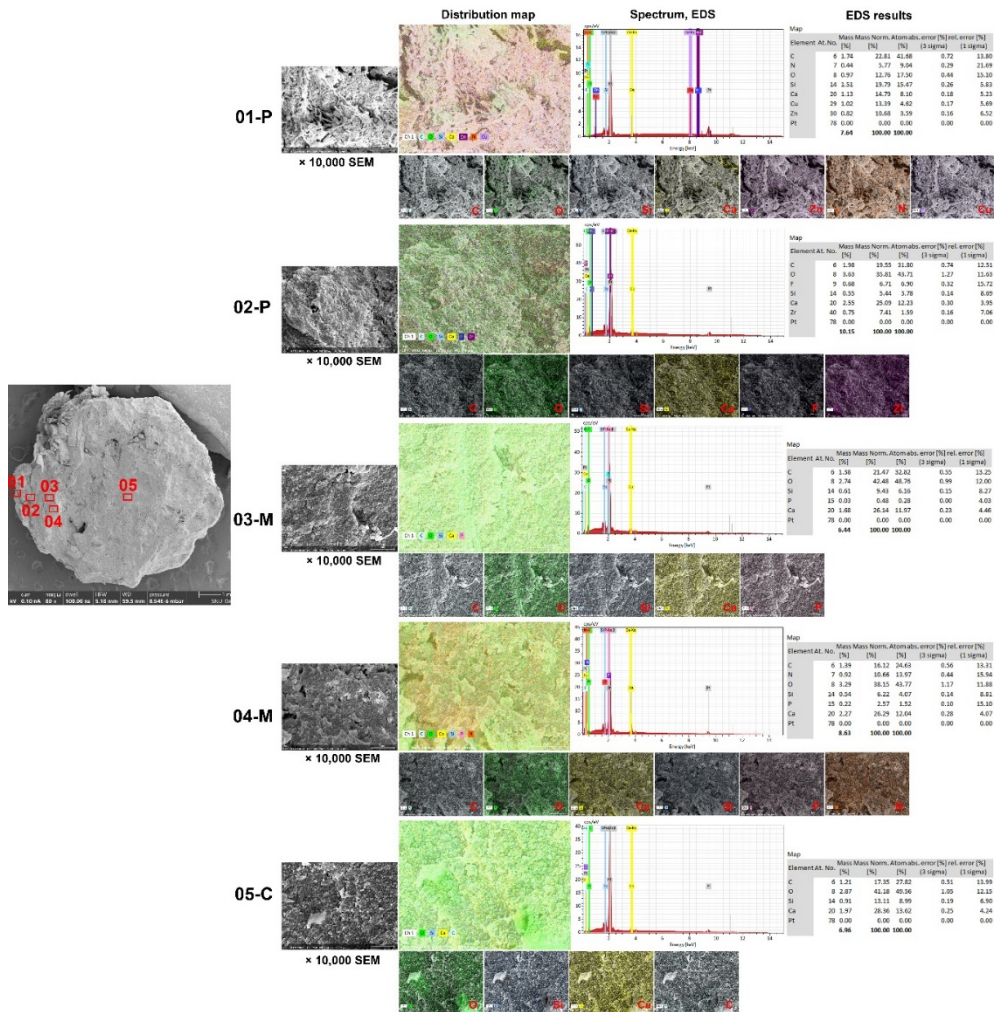
Figure 27. Mapping of elemental distribution and a spectrum of the representative points with EDS results in sialolith A14. SEM image, 10,000× magnification. EDS analyses were carried out on five representative points of interest on the peripheral (P), middle (M), and core (C) layers.
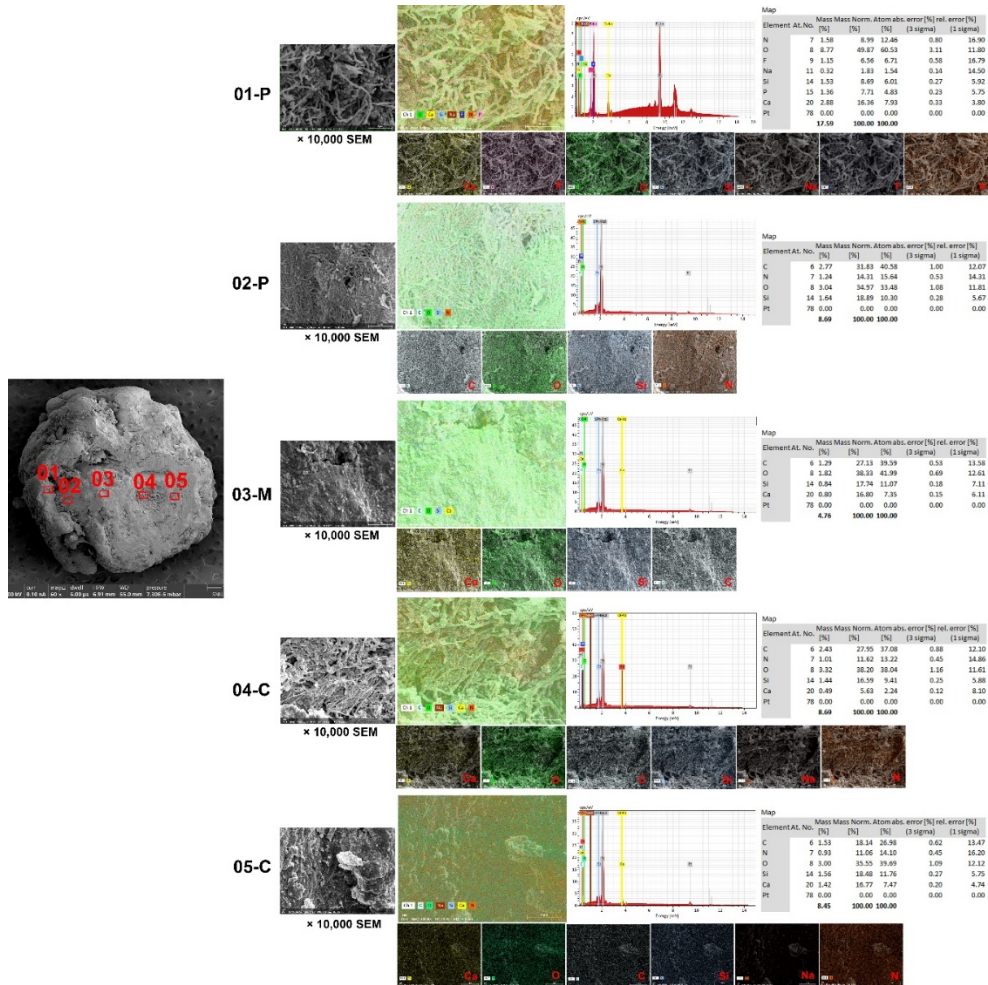
Figure 28. Mapping of elemental distribution and a spectrum of the representative points with EDS results in sialolith A17. SEM image, 10,000× magnification. EDS analyses were carried out on five representative points of interest on the peripheral (P), middle (M), and core (C) layers.
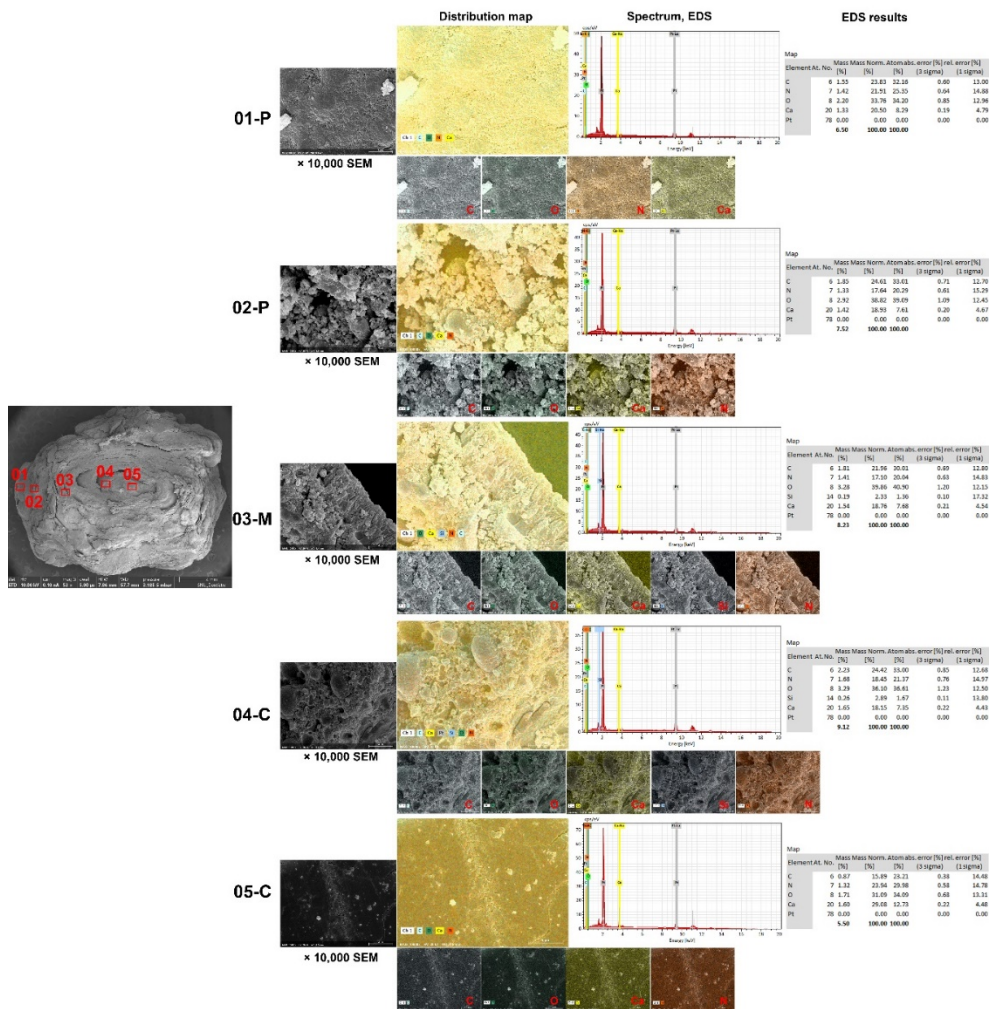
Figure 29. Mapping of elemental distribution and a spectrum of the representative points with EDS results in tonsillolith (B1). SEM image, 10,000× magnification. EDS analysis was carried out at five representative points of interest on the peripheral (P), middle (M), and core (C) layers.
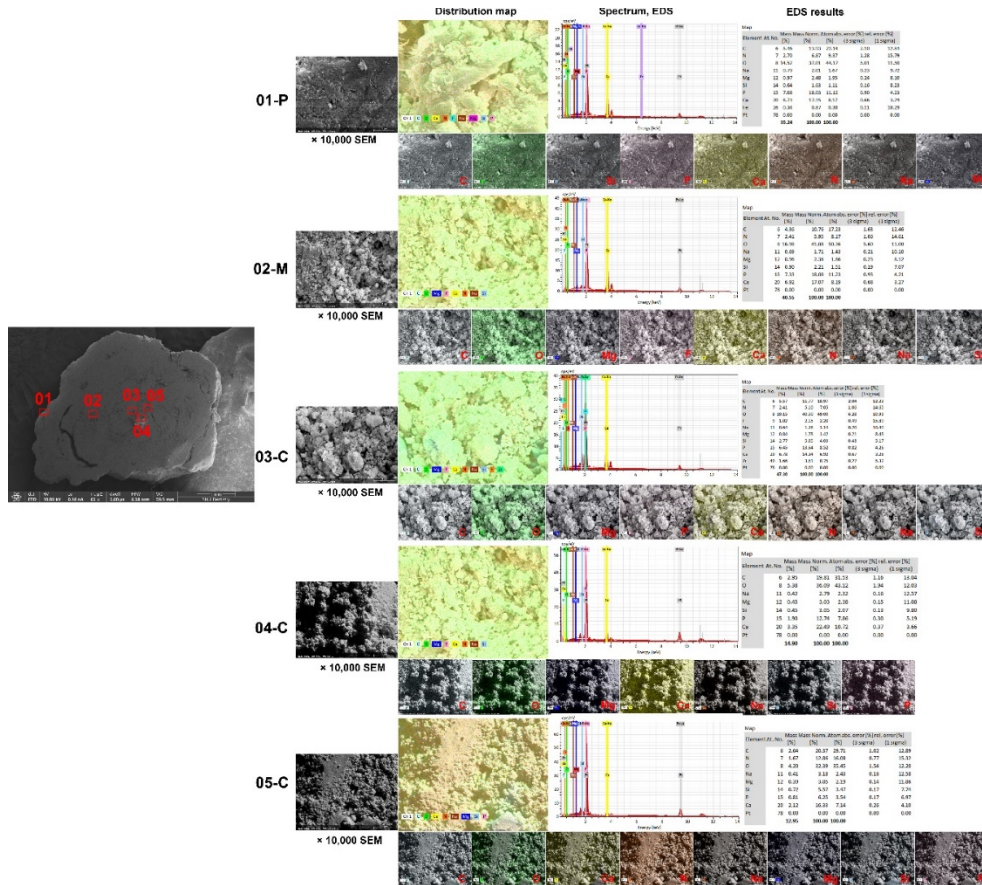
Figure 30. Mapping of elemental distribution and a spectrum of the representative points with EDS results in antrolith (C1). SEM image, 10,000× magnification. EDS analysis was carried out at three representative points of interest on the peripheral (P), middle (M), and core (C) layers.
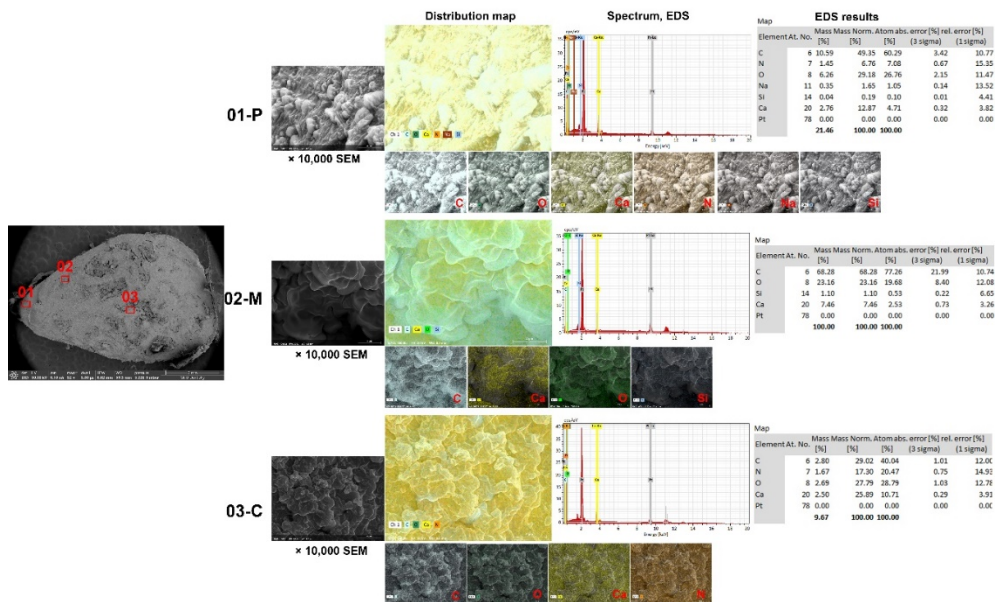
Figure 31. Mapping of elemental distribution and a spectrum of the representative points with EDS results in antrolith (C2). SEM image, 10,000× magnification. EDS analysis was carried out at five representative points of interest on the peripheral (P), middle (M), and core (C) layers.
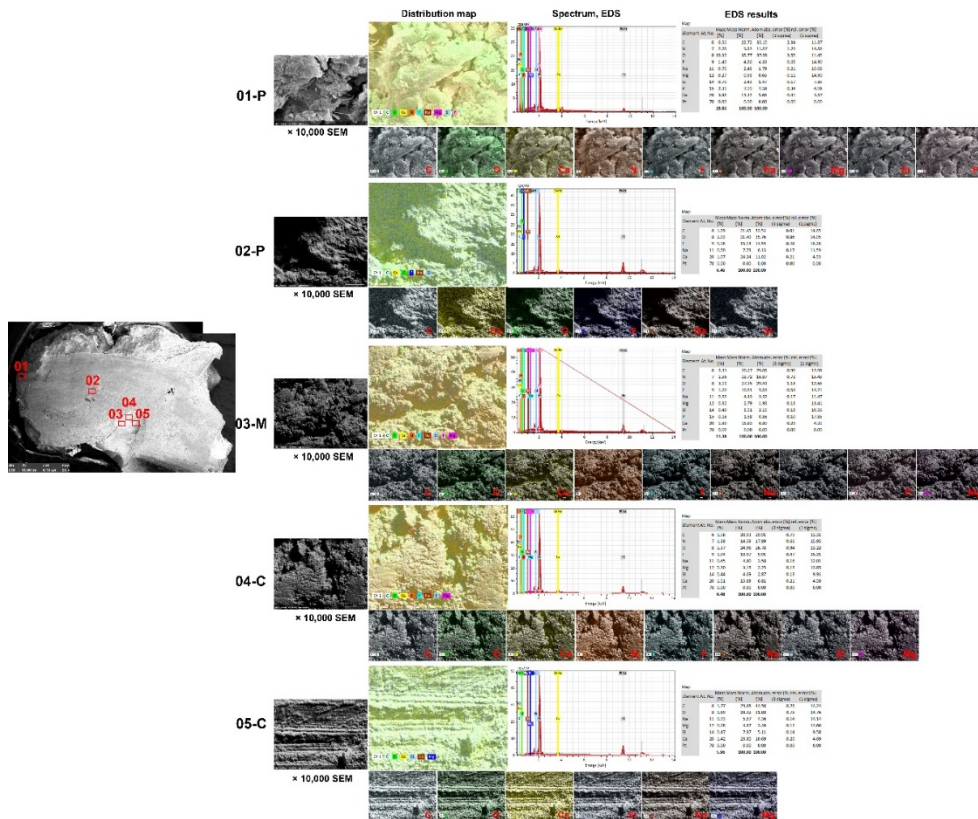
Figure 32. Representative TEM images of sialolith A6-1. Globular structures of mineralization (yellow arrowhead), magnification 2,000×, 10,000× (A-B). Lipid vesicles, magnification 2,000×, 1000× (C-D). Finger-like globular structures were found, magnification 2,000×, 10,000× (E-H).
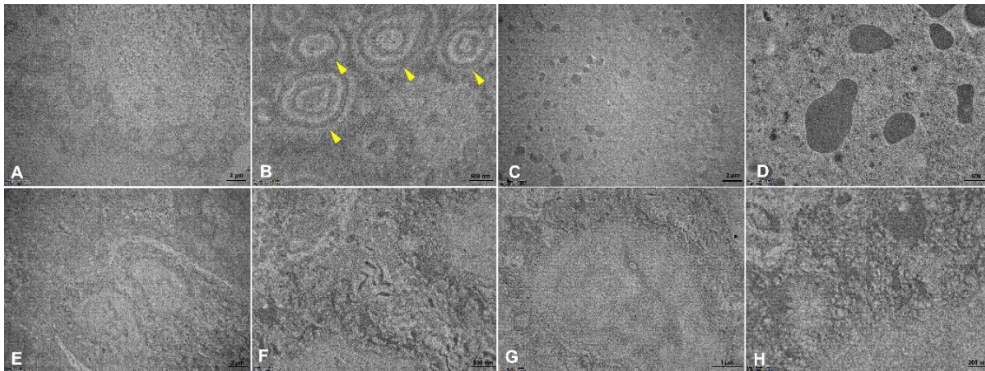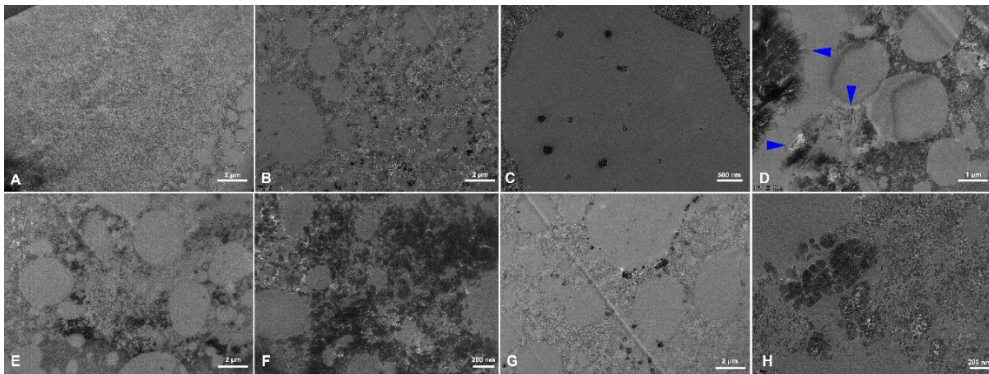
Figure 33. Representative TEM images of sialolith A6-2. Layered appearance of the sialolith showing the globular mineralized structure in internal lamella, (blue arrowheads), while the crystalline needle-like pattern was heterogeneous (yellow arrowheads), magnification 2,000×, 10,000× (A-B). Large single crystals, magnification 2,000×, 10,000× (C-D). Deposition of inorganic material (white arrows), magnification 2,000×, 10,000× (E-F). Needle-like filamentary crystals, magnification 2,000×, 20,000× (G-H).
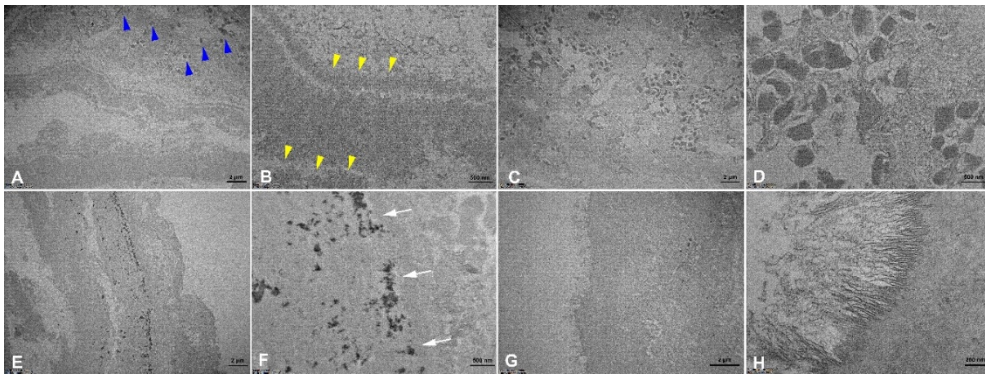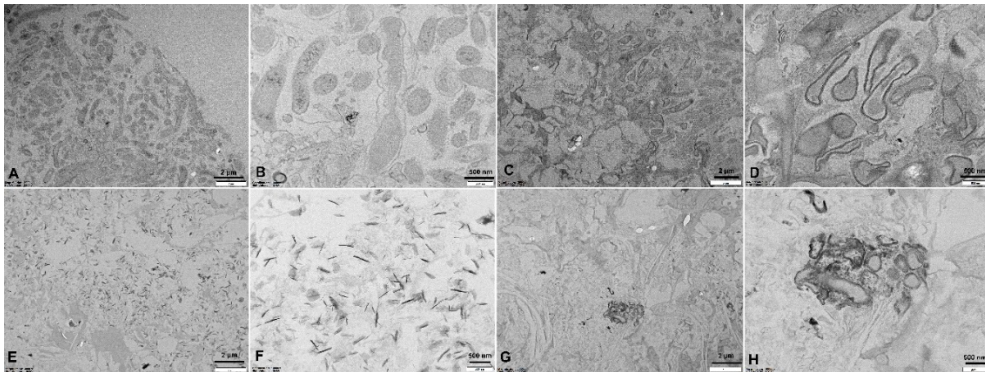
Figure 34. Representative TEM images of pediatric sialolith A13. In the internal lamellas, the globular structure was dominant (blue arrowheads), while the crystalline pattern was heterogeneous in several outer layers, with some regions of needle-like patterns (yellow arrowheads), magnification 2,000×, 6,000×, respectively (A-B). Intra-vesicular and extra-vesicular deposition of inorganic matter and large membranous bodies (white arrows), magnification 3,000×, 6,000× (C-D). Globular structures were detected in the external, magnification 3,000×, 10,000× (E-F). Globular exosomal-like structures approximately 0.5 μm in diameter were detected in the internal lamellas (red arrowheads), magnification 6,000× (G). The globular structures were noticed to have internal and surface opaque contraction. Some globular structures had double membranes (blue asterisk). Extra-vesicular deposition of inorganic matter (black arrowhead), magnification 6,000× (H).
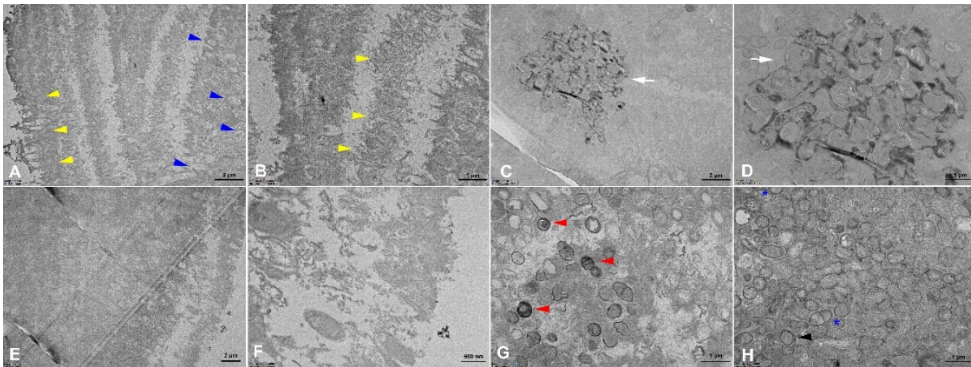
Figure 35. Representative TEM images of recurrent sialolith A17. In the peripheral lamella a homogenous layer of organic compounds was found, magnification 3,000× (A). Deposition of large single microcrystalline inorganic compounds were identified, magnification 3,000×, 10,000× (B-C). Needle-like filamentary crystals were arranged in clusters and in different directions (blue arrowhead), magnification 6,000× (D). Deposition of inorganic matter, magnification 3,000×, 20,000× (E-F). Clusters of parallelepiped crystals, magnification 3,000×, 20,000× (G-H).

Figure 36. Representative TEM images of B1 tonsillolith. In the peripheral area of the tonsillolith, stratified squamous epithelium was found, magnification 3,000×, 10,000× (A-B). Bacterial present in the middle layer of the tonsillolith, magnification 3,000×, 10,000× (C-D). Needle-like crystals in the core of the tonsillolith, magnification 3,000×, 10,000× (E-F). Extra-vesicular deposition of inorganic material, magnification 3,000×, 20,000× (G-H).

Figure 37. Representative TEM images of C2 antrolith. Outer layer showing osteoblastic rimming, magnification 3,000×, 10,000× (A-B). Dense, mature, predominantly lamellar bone in the middle area of the specimen, magnification 3,000×, 10,000× (C-D). Absence of Haversian canals and no fibrous component in the middle area of the specimen, magnification 3,000×, 10,000× (E-H).
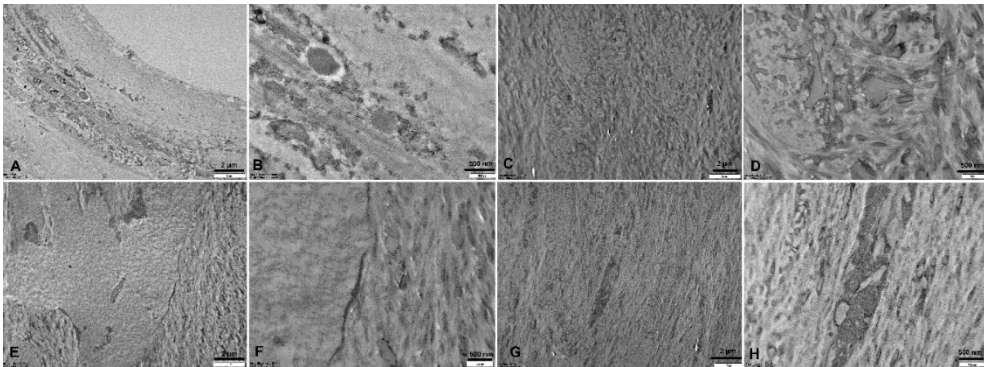
초 록

타석의 초미세구조 및 성분 분석 ; 편도석 및 상악동석과의 비교 연구

부얀빌레그

서울대학교 대학원 치의과학과 구강악안면외과전공

(지도교수 김성민)

연구의 배경 및 목적

타석증은 악하선 및 이하선 부종과 통증의 주요 원인으로 1:15,000 ~ 1:30,000 의 발병률을 보인다. 타석 형성에 대해 1) 유기적 핵심 이론: 박테리아, 이물질 또는 박리된 상피세포의 석회화; 2) sialomicrolith 이론: 일반적으로 악하선의 80% 존재하며, 3) 점액 표피 겔 이론: 고점도 뮤신의 석회화 등 많은 이론들이 제안되어 왔으나, 타석 형성의 정확한 매커니즘은

아직 알려지지 않았다. 또한 신장결석, 요결석, 담석 및 심혈관 석회화와 같은 인체의 병리학적 침착물의 특성화에 대한 많은 연구가 있지만, 타석의 초미세 구조 및 성분 구성에 대한 데이터는 매우 제한적이다.

본 연구는 편도석 및 상악동석과 비교하여 초미세 구조 및 화학 성분 분석을 수행하여 이들의 성장패턴을 파악하고, 타석 형성 및 그 합병증을 예방하기 위한 향후 중재 및 치료방법을 개발하기 위한 첫 단계가 되는 것을 목표로 하였다.

연구방법

23 명의 환자로부터 얻은 25 개의 검체를 타석(A), 편도석(B), 상악동석(C) 등 3 개의 그룹으로 분류하였다. 검체는 헤마톡실린과 에오신 염색 (H&E) 하여 광학현미경 관찰 및 micro-CT 로 상세한 특징을 분석하였고, 주사전자현미경 (SEM) 과 에너지분산 X 선분광법 (EDS) 분석을 위해 관심 영역 (ROI) 을 주변, 중간 및 코어 영역의 각 검체에 지정하여 국소 초미세 구조를 더 미세하게 분석하였다. 또한 각 그룹의 검체에 대해서 투과전자현미경 분석 (TEM) 을 수행하였다. 데이터 정규 분포는 Shapiro-Wilk 테스트되었고, 그룹 간의 차이는 일원 분산 분석을 통해 검정되었다.

연구결과

1) 마이크로 CT 분석

그룹 A 는 턱밑샘과 귀밑샘 타석 모두에서 방사선밀도층과 방사선투과층이 교대로 형성된 양파껍질과 같은 층상구조가 관찰되었다. 그룹 A 에서 11 개의 타석 검체는 하나의 코어를 가지고 있는 반면, 하나의 타석은 여러 개의 코어를 가지고 있고, 다른 하나는 두 개의 코어를 가지고 있었으며, 또 다른 하나는 뚜렷한 코어가 관찰되지 않았다. 또한 그룹 A 타석은 구형의 타원형 또는 비대칭적인 모양을 가지고 있었으며, 타석의 코어는 주변 층에 비해 광물화 정도가 뚜렷하게 높거나 낮았다. 그룹 B 는 동심 적층 패턴이 없는 균질한 구조를 보였다. 그룹 C 는 그룹 A 와 그룹 B 에 비해 내부 공극이 더 많은 치밀한 균질 구조를 보였다. 각 그룹은 total VOI (volume of interest) volume, object volume, percent object volume, total VOI surface, object surface, object surface/ volume ratio, object surface density, structure thickness, structure separation 및 total porosity (%)의 다른 형태학적 매개변수를 나타내었지만 통계적으로 유의한 차이는 발견되지 않았다.

2) 병리조직학적 분석

그룹 A 는 유기물과 무기물의 동심원 라멜라 구조를 보였다. 코어에서 호산구성 특성을 보였고, 주변부에서 눈물방울 모양의 구형 구조의 적층 패턴을 보였다. 그룹 B 는 섬유소 잔해와 염증 세포로 둘러싸인 성숙한 발달 단계를 보여주었다. 작은 타액선 관을 나타내는 편평 상피의 중심에서 덕트형 구조가 관찰되었고, 편도석 표면의 편평 상피는 편도선와 (tonsil

crypt) 의 내벽을 향해 확장되는 것으로 나타났다. 그룹 C 에서 병변은 캡슐화되지 않았으며 섬유성 골수강이 있는 균질한 층상골이 관찰되었다.

3) 주사전자현미경(SEM) 분석

SEM 결과에서 그룹 A 의 일반적인 구조는 광물화된 물질과 유기물질이 번갈아 나타나는 동심원의 라멜라 구조가 관찰되었고, 재발된 타석 검체(A17)에서는 타석의 중심부에서 이물인 diatomite 입자가 발견되었다. BSE 모드는 전자 후방 산란 확률이 시료 원소의 원자 질량에 비례하기 때문에 각 층의 서로 다른 화학 조성을 비교할 수 있게 하였다. 각 층의 미세구조는 다양한 크기와 정도의 광물화된 구상체로 나사산으로 되어 있었다.

4) 에너지분산X선분광법 (EDS) 분석

각 검체의 조성 분석 결과 그룹 A, B 및 C 에서 칼슘(Ca), 탄소(C), 산소(O)의 높은 비율의 일관된 화학 성분을 보여주었다. 그룹 A 는 그룹 C (14.78±10.29 wt% 및 5.76±4.52 at%) 에 비해 Ca Wt% (20.50±6.28 wt% and 16.74±44.08 at%) 의 수준이 유의하게 높았다 (p=0.003). 그룹 C 는 그룹 A (22.48±11.08wt%, 33.64±6.36at%) 에 비해 C 그룹 (49.27±20.21wt%, 49.27±20.21at%) 에서 더 높았으나 유의한 차이는 없었다. O 의 wt% 및 at%는 그룹 A (36.46±8.16 wt% 및 40.12±8.93 at%) 가 그룹 C (27.18±2.37 wt% 25.36±4.29 at%) 에 비해 유의하게 높았다 (p=0.002; p=0.019).

질소(N), 나트륨(Na), 규소(Si)를 포함한 다른 원소들은 두 그룹 모두에서 검출되었고, 구리(Cu), 불소(F), 인(P), 아연(Zn) 및 지르코늄(Zr)은 그룹 A 에서만 발견되었으며, 그룹 C 에서는 이러한 원소가 나타나지 않았다. 그룹 C (49.23±20.22wt%, 59.23±18.68at%) 는 그룹 A (22.36±4.70wt%, 32.46±5.74at%) 에 비해 그룹 C 에서 유의하게 높았다 (p=0.00; p=0.035).

5) 투과전자현미경 (TEM) 분석

그룹 A 에서 이중막을 갖는 구형 구조물이 수포 내 석회화를 겪는 것으로 관찰되었고, 지질 소포와 손가락 모양의 구형 구조도 관찰되었다. 바늘 모양의 필라멘트 결정은 수산화인회석 구조를 시사하였고, 무기물의 수포내 및 수포외 침착이 관찰되었다.

결론

본 연구에서는 구강악안면외과 분야에서 발견되는 석회화의 다양한 유형 간 비교로 미세구조 및 구성 성분 연구를 수행하였다. 이 연구는 Micro-CT, SEM, EDS 및 TEM 분석을 통해 타석, 편도석 및 상악동석의 원소 조성이 서로 완전히 다른 미세 형태를 가지고 있음을 보여주었다.

타석은 고도로 광물화되거나 덜 광물화 된 코어를 가진 동심 적층 구조를 가지고 있는 반면, 편도석과 상악동석은 코어가 부족하였고, 상악동석은 층상골과 유사한 구조와 구성을 보였다. 이러한 결과는 각

유형의 석회화에서 서로 다른 석화 형성을 시사하며, 이는 각 유형의 석회화에서 서로 다른 치료 양식을 개발하는 근본적인 단계가 될 수 있다.

중심어: 결석증, 마이크로 컴퓨터 X-선 단층 촬영, 조직병리학, 주사전자현미경, 에너지 분산형 X 선 분광기, 투과전자현미경

학번: 2021-36814

Acknowledgements

I would like to express my sincere gratitude and warm appreciation to the Department of Oral and Maxillofacial Surgery, School of Dentistry, Seoul National University for giving me this rare and wonderful opportunity to study here. I am most thankful to a number of people, who has given me support and encouragement during the preparation of this thesis.

First and foremost, I am extremely grateful to my mentor Prof. Soung Min Kim for his continuous support in my study as a clinician and a researcher, for his generous patience, knowledge, enthusiasm and most importantly in his belief in me. Words can only inadequately express my gratitude to my mentor Prof, as his guidance and professional attitude has helped me greatly to carry out this study. I could not have imaged having a better mentor and advisor than Prof.

Thank you, my beloved Lab members, Ms. Mi Young Eo, Ms. Yun Ju Cho, Ms. Jin Hee Kim, Ms. Ji-Hye Oh, Ms. Yun Ju Kim, Dr. Ju Young Lee, Mr. Young Hwan Choi, Dr. Truc Thi Hoàng Nguyen, and Dr. Kezia Rachellea Mustakim. Your warm and welcoming kindness, companionship and encouragement has made my life in Korea most valued and precious time. I had the great privilege to be a part of the Lab.

The honorable Professors in the Department of Oral and Maxillofacial Surgery, Prof. Jong-Ho Lee, Prof. Jin-Young Choi, Prof. Byoung-Moo Seo, Prof. Hoon Myoung, Prof. Joo-Young Park, Prof. Mi Hyun Seo, Prof. Hoon-Joo Yang, Prof. Ik-Jae Kwon,

Prof. Jeong-Jun Han and Prof. Won Jae Choi. Thank you so much for the knowledge you have passed on and I will always be grateful for the having the opportunity study under your kind guidance for four brilliant years.

My loving and caring parents, Sodnom-Ish Tseveg and Khishigjargal Bataa, I am grateful for your selfless love and hard work dedicated for your children. You have always been the role model and the driving force of my life. And my brother, Buyandelger Sodnom-Ish, thank you always for your encouragement and moral support.

24th Jan. 2023.

Buyanbileg Sodnom-Ish